



Hysteretic Beam Finite-Element Model Including Multiaxial Yield/Capacity Surface Evolution with Degradations

M. Amir, S.M.ASCE¹; K. G. Papakonstantinou, M.ASCE²; and G. P. Warn, A.M.ASCE³

Abstract: A multiaxial degrading hysteretic model is developed, enabling consistent multiaxial yield/capacity surface evolution with degradations, and is appropriately incorporated in a finite-element framework using hysteretic Timoshenko beam elements. Degradation phenomena are introduced in this model in the form of either symmetric or asymmetric strength degradation, stiffness degradation, pinching functions, and various combinations thereof. More specifically, a new strength degradation function is developed and enhancements in other existing functions are suggested to simulate the physically observed degradation phenomena in structural elements. The degradation functions are then employed in a multiaxial classical damage-plasticity framework to satisfy the consistency criterion of the yield/capacity surface, thereby resulting in a set of new multiaxial hysteretic evolution equations. The proposed evolution equations are specifically formulated so as they could be seamlessly incorporated into a hysteretic finite-element formulation, using appropriate displacement and hysteretic interpolation functions, to satisfy the exact equilibrium conditions and model distributed plasticity characteristics, thereby avoiding any shear locking effects. As such, the proposed hysteretic finite-element model accounts for equilibrium, distributed plasticity, degradations, and multiaxial inelasticity with capacity interactions in a single consistent and unified framework. Constant system matrices are employed that do not require updating throughout the analysis, while the degradations and inelasticity are captured through the suggested multiaxial hysteretic evolution equations. An efficient numerical solution scheme is also devised, where the finite-element model can be expressed explicitly in terms of first order ordinary differential equations (ODEs), rather than a set of complex differential-algebraic equations for quasi-static cases. The resulting system of equations can be then straightforwardly solved using any standard ODE solver, without any required linearization. Numerical illustrations and experimental verifications are provided to demonstrate the performance and utility of the suggested methodology. DOI: 10.1061/(ASCE)EM.1943-7889.0001767. © 2020 American Society of Civil Engineers.

Introduction

A hysteretic beam finite-element modeling approach with a new multiaxial yield/capacity surface evolution criterion for degrading structural elements is presented. Three primary contributions enabling this consistent and unified modeling framework are described herein. First, a uniaxial degrading hysteretic model is developed to simulate highly nonlinear and degrading behaviors physically observed in structural elements after extreme loading events. Second, the suggested uniaxial model is extended in a multiaxial plasticity framework, using a damage-plasticity approach, that satisfies the classical plasticity postulates and the consistency criteria of the yield/capacity surface, thus resulting in a consistent multiaxial degrading hysteretic model. Third, the developed multiaxial model is employed for the finite-element formulation of a nonlinear Timoshenko beam element to realize a degrading hysteretic beam finite-element model. In addition to this model, a numerical solution scheme is also suggested, where the entire finite-element

¹Graduate Student Researcher, Dept. of Civil and Environmental Engineering, Pennsylvania State Univ., University Park, PA 16802 (corresponding author). Email: mza40@psu.edu

Note. This manuscript was submitted on May 14, 2019; approved on December 3, 2019; published online on July 10, 2020. Discussion period open until December 10, 2020; separate discussions must be submitted for individual papers. This paper is part of the *Journal of Engineering Mechanics*, © ASCE, ISSN 0733-9399.

formulation is presented concisely as a system of ordinary differential equations (ODEs), that can be efficiently solved without the need of linearization techniques. Thus, an alternative approach to traditional nonlinear structural analysis techniques, such as solid finite elements, fiber-based approaches, and discrete plasticity with nonlinear spring models (Spacone et al. 1996; Scott et al. 2008; Lignos and Krawinkler 2010; Deierlein et al. 2010), is presented in this work, incorporating distributed plasticity, multiaxial interactions, and combined degradation-plasticity phenomena, among others, in an efficient and unified framework.

Smooth hysteretic models for uniaxial systems can be seen in early developments by Bouc (1967) and Wen (1976), where the main idea is to express the evolution of hysteresis in the form of first order ODEs, commonly referred to as evolution equations. Following these early developments and recognizing the potential for modeling a variety of physically observed phenomena in structural elements, other works (Baber and Wen 1981; Baber and Noori 1985; Foliente 1995; Sivaselvan and Reinhorn 2000; Wang et al. 2001; Ibarra et al. 2005) introduced strength degradation, stiffness degradation, pinching, and asymmetric yielding, by means of suitable degradation functions for uniaxial hysteresis, and Charalampakis and Koumousis (2009) and Kottari et al. (2014) have shown the capability of such uniaxial hysteretic models to fully satisfy Drucker or Ilyushin conditions of plasticity, including for short unloading-reloading paths. These and other hysteretic variants, e.g., Papakonstantinou et al. (2008), Miah et al. (2015), among others, have been extensively used in various applications to simulate the response of a diverse array of materials and structural components/devices, as summarized in Ismail et al. (2009). These models are mainly of a phenomenological nature, and the progression in this work is toward a model based on multiaxial classical plasticity and damage theories, as described in detail subsequently.

²Assistant Professor, Dept. of Civil and Environmental Engineering, Pennsylvania State Univ., University Park, PA 16802. Email: kpapakon@psu.edu

³Associate Professor, Dept. of Civil and Environmental Engineering, Pennsylvania State Univ., University Park, PA 16802. Email: gpw1@psu.edu

In the original formulation of Baber and Wen (1981), the strength degradation is defined by a linearly increasing function of the energy dissipated by the hysteretic model, referred to herein as linear-rate strength degradation function, which can be appropriately incorporated into a uniaxial degrading hysteretic evolution equation and a relevant finite-element framework. Recent applications of the linear-rate strength degradation function can be found in Sengupta and Li (2013), Yu et al. (2016), and Sofianos and Koumousis (2018), among others. However, structural behavior does not often adhere to this idealization; for instance, strength degradation might initiate after several inelastic cycles and then rapidly increase prior to failure, suggesting a rate that is naturally not linear. As such, an alternative strength degradation function is suggested here that is able to simulate a broader range of commonly observed degradation types. In addition, the pinching function of Foliente (1995) is simplified to reduce the number of parameters, without compromising its capability of simulating a diverse range of pinching phenomena. Lastly, asymmetry in stiffness and in other degradation effects is also considered. The resulting degradation functions are all combined to develop a new uniaxial degrading hysteretic model that is able to simulate strength degradation, stiffness degradation, pinching, and the associated degradation asymmetries in a single parametrized expression.

The suggested degrading uniaxial hysteretic model is then effectively incorporated into a multiaxial plasticity framework. Hysteretic models in a multiaxial plasticity context have been suggested by Casciati (1989), Sivaselvan and Reinhorn (2004), and Triantafyllou and Koumousis (2011a), among others, where the model is elegantly formulated based on the multiaxial classical plasticity postulates (see Appendix II for a detailed presentation of this fact). However, important observed degradation phenomena have yet to be adequately integrated with these available multiaxial models, without violating the consistency condition of the capacity surface in the inelastic domain, due to the strength degradation capacity change. Therefore, strength degradation is consistently treated as a scalar damage function in this paper, and the multiaxial degrading hysteretic model/law is formulated in the effective stress domain by employing notions of continuum damage mechanics, so as to satisfy the plasticity postulates and consistency criteria of the yield/capacity surface for a degrading system.

The concept of continuum damage theory and scalar damage function was pioneered by Kachanov (1958) to measure the density of microcracks/microvoids and their influence on the material behavior. This idea is extensively used in the field of solid mechanics and has been successfully adapted for plasticity theory, resulting in coupled damage-plasticity models (Lemaitre 1985; Lemaitre 1996; Krajcinovic 1996). Numerous applications can be seen for both solid finite-element and fiber based damage frameworks of structures (Lubliner et al. 1989; Grassl and Jirásek 2006; Andriotis et al. 2015; Van Do 2016; Feng et al. 2017, 2018; Di Re et al. 2018; Do and Filippou 2018). The concept of scalar damage function is employed here to suggest a new multiaxial degrading hysteretic model, thus resulting in new multiaxial evolution equations with coupled degradation-plasticity effects. These developed hysteretic evolution equations have the important attribute of being derived from the physics of classical multiaxial plasticity to satisfy the loading rate, the yield/capacity criterion, and the flow rule, and can compactly and seamlessly describe loading, unloading, and reloading of a hysteretic cycle in merely a single vectorized differential equation expression.

The suggested multiaxial hysteretic evolution equations are then employed for the formulation of a degrading hysteretic beam finite-element model, the consistent nonlinear Timoshenko beam element, suggested in Amir et al. (2020). In the pertinent beam element formulation, multiaxial interactions are accounted for through yield/capacity functions, and distributed plasticity is described using appropriate hysteretic interpolation functions. The suggested model in Amir et al. (2020) does not, however, consider degradation effects in the element. By employing the herein suggested consistent multiaxial degrading hysteretic model/laws, the finite-element model is thus significantly extended and enabled to simulate a wide range of plasticity and degradation phenomena, as illustrated through numerical examples and experimental verifications. Additionally, all the capabilities of the hysteretic element in Amir et al. (2020) are preserved in the present formulation, including its computational efficiency, primarily due to the fact that the elastic and hysteretic matrices remain constant, and both need to be evaluated only once at the beginning of the analysis, given that the nonlinearities and degradation effects are captured through local evolution equations. The hysteretic finite-element formulation can be thus conveniently presented in state-space form for dynamic cases, as shown in Triantafyllou and Koumousis (2011a, b), and can be efficiently solved using common ODE solvers. The solution of quasi-static problems, however, is less straightforward due to the presence of complex and hard to solve differential algebraic equations (DAEs), requiring both differential and algebraic forms to be solved simultaneously. Addressing this issue, an alternative solution scheme, similar to Amir et al. (2020), aimed to efficiently solve quasi-static problems is presented here for the paper completeness.

In the remainder of this paper, the formulation and consistency of the hysteretic beam finite-element model, along with its solution scheme at the system level, are explained in detail through mathematical expressions and illustrative examples. Finally, model performance, versatility, and validity are demonstrated through several comparisons with experimental data from available tests.

Degrading Hysteretic Laws: Uniaxial Case

This section briefly reviews the existing uniaxial degrading hysteretic models/laws and describes in detail the suggested enhancements to incorporate several physically observed structural degradation phenomena. A uniaxial law in terms of moment-curvature is shown here to illustrate the degrading hysteretic formulation, realizing that the concept can be readily employed for any other work conjugate pair. Accordingly, a common moment (M)-curvature (ε_{ϕ}) uniaxial degradation hysteretic law found in the literature (Baber and Wen 1981; Baber and Noori 1985; Foliente 1995; Wang et al. 2001) can be expressed as:

$$\begin{split} M &= \alpha_{\phi} E I \varepsilon_{\phi} + (1 - \alpha_{\phi}) E I z_{\phi} \\ \dot{z}_{\phi} &= \frac{h_{\phi}}{\eta_{\phi}} \left(1 - \nu_{\phi} \left| \frac{M^{h}}{M_{c}^{h}} \right|^{n} (\beta + \gamma \operatorname{sgn}(M^{h} \dot{\varepsilon}_{\phi})) \right) \dot{\varepsilon}_{\phi} \end{split} \tag{1}$$

where $M^h=(1-\alpha_\phi)EIz_\phi$ represents the hysteretic component of the bending moment; $M_c^h=(1-\alpha_\phi)M_p$ is the hysteretic bending capacity; M_p is an estimated plastic moment capacity; E is the elastic modulus; I is the moment of inertia; z_ϕ is the hysteretic curvature; α_ϕ is the post-elastic to elastic stiffness ratio; h_ϕ , η_ϕ , and ν_ϕ are the pinching, stiffness degradation, and strength degradation functions, respectively, due to flexure; β , γ , n are the model parameters; sgn(.) is the signum function and the overdot indicates differentiation with respect to time. Parameter n controls the smoothness of the transition from the elastic to the inelastic regime, whereas parameters β and γ control the shape of the hysteretic loops. Furthermore, for Eq. (1) to be thermodynamically admissible, $\beta+\gamma=1$ and $-\gamma \leq \beta \leq \gamma$ (Erlicher and Point 2004).

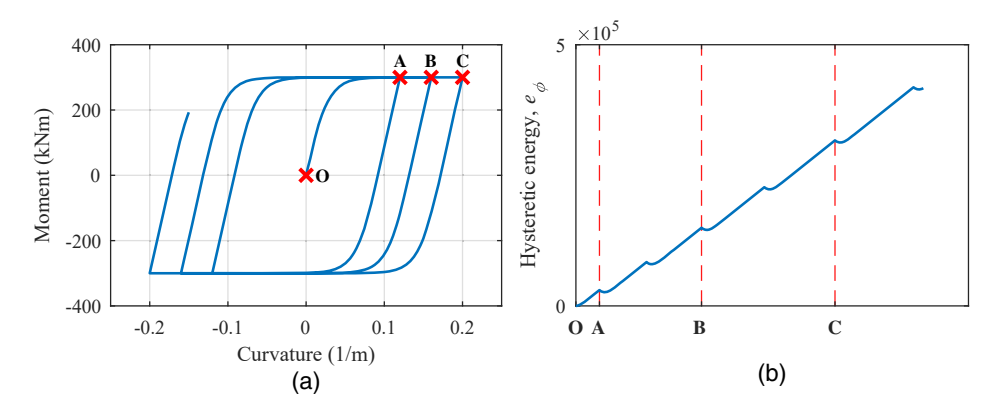


Fig. 1. A Nondegrading hysteretic response for cyclic loading.

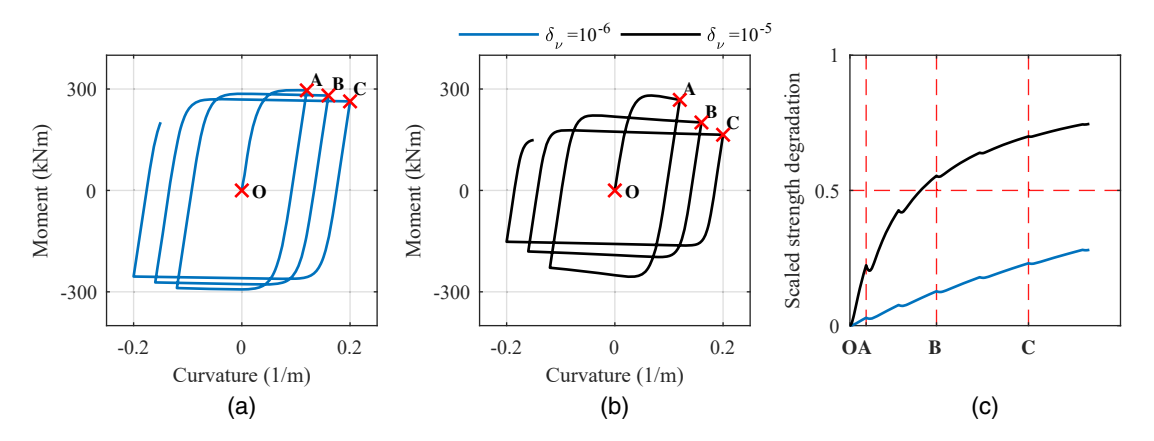


Fig. 2. Response of a linear-rate strength degradation function for different parameter values.

The degradation functions are formulated such that their values are equal to 1 when there is no respective degradations in the system, as also presented in Fig. 1. Fig. 1(a) is an illustrative localized moment-curvature response obtained using Eq. (1) with $\nu_{\phi} = \eta_{\phi} = h_{\phi} = 1$, for three loading-unloading cycles with increasing curvature amplitude for each subsequent cycle. The specified parameters for this illustration are: $\alpha_{\phi} = 0$, $E = 2 \times$ 10^{11} N/m^2 , $I = 5,290 \text{ cm}^4$, $M_p = 300 \text{ kNm}$, n = 2, and $\beta = \gamma =$ 0.5. The cumulative dissipated hysteretic energy, $e_{\phi} = \oint M^h d\varepsilon_{\phi}$, is shown in Fig. 1(b), where ϕ indicates integration over the hysteretic cycles. In Fig. 1, point O is the origin and points A, B, and C are the steps corresponding to maximum positive curvature values for each cycle. As can be seen from the results in Fig. 1, the hysteretic behavior is smooth and without degradation. In the subsequent subsections, different degradation functions are described in detail.

Proposed Strength Degradation Function

As previously mentioned, existing strength degradation formulations found in the literature (Baber and Wen 1981; Baber and Noori 1985; Foliente 1995) are based on the assumption that the rate of degradation is linearly proportional to the rate of hysteretic energy dissipation, and thus can be expressed as:

$$\nu_{\phi} = 1 + \delta_{\nu} e_{\phi} \tag{2}$$

where δ_{ν} is a scaling parameter corresponding to the strength degradation, such that there is no strength degradation for $\delta_{\nu}=0$, whereas degradation effects can be magnified by assigning a larger parameter value. For the benefit of the subsequent discussion, the outcome of the linear-rate degradation on the hysteretic response is illustrated in Fig. 2, obtained by substituting Eq. (2) into Eq. (1) and specifying $\eta_{\phi}=h_{\phi}=1$. Figs. 2(a and b) show the simulated moment-curvature responses for different values of δ_{ν} , to illustrate the impact of the degradation parameter on the hysteretic response, and Fig. 2(c) represents the corresponding scaled value of the strength degradation function, given by:

$$d_{\phi} = 1 - \frac{1}{\nu_{\phi}} \tag{3}$$

where $d_\phi \in [0\,1)$, with the bounding values corresponding to no degradation and full degradation, respectively. As seen in Fig. 2, moment degradation is increased by increasing the parameter value from 10^{-6} in Fig. 2(a) to 10^{-5} in Fig. 2(b). Fig. 2(c) also shows that the increase in parameter value increases the curvature/convexity of the scaled function, resulting in greater initial degradation, indicated by the region OA. Thus, the function in Eq. (2) has a significant impact on the initial strength degradation of the system. Yet, experimental observations suggest that degradation is often low/small during initial low amplitude cycles, and then increases with increasing amplitude cycles. This phenomenon can not be then simulated with the mathematical form of the existing function in Eq. (2).

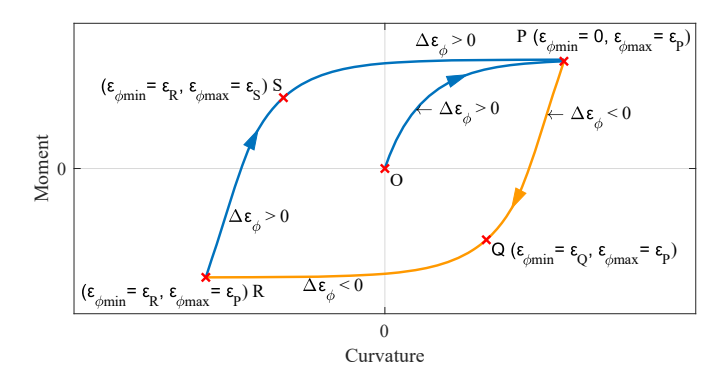


Fig. 3. Localized curvature values for different branches.

In order to simulate these often experimentally observed degradation types, as well as the linear-rate degradation, an alternative degradation function is introduced:

$$\nu_{\phi} = 1 + \delta_{\nu 1} [\exp(\delta_{\nu 2} e_{\phi}) ((\varepsilon_{\phi} - \varepsilon_{\phi_{\rm Deak}}) {\rm sgn}(\Delta \varepsilon_{\phi}) + 1)^{\delta_{\nu 3}} - 1] \eqno(4)$$

where $\delta_{\nu 1}$, $\delta_{\nu 2}$, and $\delta_{\nu 3}$ are the time invariant parameters controlling different strength degradation phenomena; $\Delta \varepsilon_{\phi} = (\varepsilon_{\phi} - \varepsilon_{\phi_0})$ is the change in curvature; ε_{ϕ_0} indicates the curvature from the previous solution step; and $\varepsilon_{\phi_{\rm peak}}$ is the *localized peak* curvature for each loading/unloading branch. The value of $\varepsilon_{\phi_{\rm peak}}$ at each step can be efficiently updated using the following equations:

$$\begin{split} \varepsilon_{\phi_{\min}} &= c(\Delta\varepsilon_{\phi})\varepsilon_{\phi_{\min0}} + c(-\Delta\varepsilon_{\phi})\varepsilon_{\phi} \\ \varepsilon_{\phi_{\max}} &= c(-\Delta\varepsilon_{\phi})\varepsilon_{\phi_{\max0}} + c(\Delta\varepsilon_{\phi})\varepsilon_{\phi} \\ \varepsilon_{\phi_{\text{peak}}} &= c(\Delta\varepsilon_{\phi})\varepsilon_{\phi_{\min}} + c(-\Delta\varepsilon_{\phi})\varepsilon_{\phi_{\max}} \end{split} \tag{5}$$

where $\varepsilon_{\phi_{\min}}$, $\varepsilon_{\phi_{\max}}$, and $\varepsilon_{\phi_{peak}}$ are the localized minimum, maximum, and peak curvatures at the current step; and $\varepsilon_{\phi_{\min}}$ and $\varepsilon_{\phi_{\max}}$ correspond to the minimum and maximum curvatures at the beginning of each solution step. Function c(t), introduced in Eq. (5), is a Heaviside function, defined as:

$$c(t) = \frac{1 + \operatorname{sgn}(t)}{2} \tag{6}$$

Note that the curvature values in Eq. (5) are not the absolute maximum and minimum from the complete analysis but rather the localized values corresponding to each branch of the current cycle. For the unloading cycle, when $\Delta\varepsilon_{\phi}\leq 0$, Eq. (5) results in $\varepsilon_{\phi_{\min}}=\varepsilon_{\phi}$, $\varepsilon_{\phi_{\max}}=\varepsilon_{\phi_{\max}}$, and $\varepsilon_{\phi_{\mathrm{peak}}}=\varepsilon_{\phi_{\max}}$, implying that the peak curvature for the unloading branch is equal to the maximum curvature obtained for that branch. Similarly, for the loading/reloading cycle, when $\Delta\varepsilon_{\phi}\geq 0$, Eq. (5) results in $\varepsilon_{\phi_{\min}}=\varepsilon_{\phi_{\min}}$, $\varepsilon_{\phi_{\max}}=\varepsilon_{\phi}$, and $\varepsilon_{\phi_{\mathrm{peak}}}=\varepsilon_{\phi_{\min}}$, indicating that the peak curvature for the loading/reloading is equal to the minimum curvature obtained for that branch. This is illustrated in Fig. 3, where the minimum and maximum curvature values at step Q are equal to curvature values at Q and P, respectively, and the resulting peak curvature at Q is equal to the curvature value obtained at P. Similarly, according to Eq. (5), for the illustrative example in Fig. 3, the values of $\varepsilon_{\phi_{\mathrm{peak}}}$ for each branch are summarized as:

$$\begin{aligned} OP\left(\Delta\varepsilon_{\phi} > 0\right) &: \varepsilon_{\phi_{\text{peak}}} = \varepsilon_{\phi_{\text{min}}} = \varepsilon_{\phi(O)} \\ PQR\left(\Delta\varepsilon_{\phi} < 0\right) &: \varepsilon_{\phi_{\text{peak}}} = \varepsilon_{\phi_{\text{max}}} = \varepsilon_{\phi(P)} \\ RSP\left(\Delta\varepsilon_{\phi} > 0\right) &: \varepsilon_{\phi_{\text{peak}}} = \varepsilon_{\phi_{\text{min}}} = \varepsilon_{\phi(R)} \end{aligned} \tag{7}$$

where $\varepsilon_{\phi(O)}$, $\varepsilon_{\phi(P)}$, and $\varepsilon_{\phi(R)}$ are the curvature values at points O,P, and R, respectively. Therefore, by employing Eq. (5), peak curvature values can be continuously updated based only on the previous and current states without requiring the entire history to be stored in memory.

The proposed strength degradation function in Eq. (4) is formulated such that it consists of a hysteretic energy based component, indicated by the first term in the square parentheses, as well as a strain-based component, indicated by the second term in the square parentheses. For completeness, details pertaining to the formulation of this degradation function, its application, and the effect of different parameters are described in the following subsections.

Hysteretic Energy Based Component

The influence of the cumulative hysteretic energy dissipation on the strength degradation can be illustrated by setting the parameter $\delta_{\nu 3}=0$, such that the expression given in Eq. (4) reduces to Eq. (8):

$$\nu_{\phi} = 1 + \delta_{\nu 1} [\exp(\delta_{\nu 2} e_{\phi}) - 1]$$
 (8)

Eq. (8) is similar to Eq. (2), in the sense that strength degradation is again increasing with increasing hysteretic energy dissipation; however, instead of linear-rate, exponential growth rate of degradation with respect to energy is introduced here to simulate the aforementioned effects. The value in the parenthesis, i.e., $[\exp(\delta_{\nu 2}e_{\phi}) - 1]$, determines the degradation evolution depending on $\delta_{\nu 2}$ values, where the lower bound is always 0 irrespective of the value of $\delta_{\nu 2}$; however, the upper bound increases exponentially with the parameter $\delta_{\nu 2}$. For example, with smaller values of $\delta_{\nu 2}$, almost linear evolution is obtained; however, by increasing the value of $\delta_{\nu 2}$, the nonlinearity in the rate of degradation growth is increased. Additionally, $\delta_{\nu 1}$ is a scaling parameter that predominantly controls the onset of degradation; for example, with a very small value of $\delta_{\nu 1}$, degradation is delayed, because even though the e_{ϕ} values are increasing in time, $\delta_{\nu 1}$ scales down the function value, resulting in a delay in the initiation of the degradation, while after the onset, the degradation evolution is controlled by the parameter $\delta_{\nu 2}$. Therefore, by the combination of $\delta_{\nu 1}$ and $\delta_{\nu 2}$ values, different degradation profiles can be achieved based on the material behavior.

The effect of parameter $\delta_{\nu 1}$ can be seen in Fig. 4, where Figs. 4(a and b) show the moment-curvature responses for $\delta_{\nu 1}=1$ and $\delta_{\nu 1} = 0.01$, respectively, both with $\delta_{\nu 2} = 1.5 \times 10^{-5}$, and Fig. 4(c) gives the scaled degradation evolution for both considered parameter values. In Fig. 4(a), it can be observed that the value of moment at A is less than the initial moment capacity of 300 kNm, and the capacity further reduces in each of the subsequent cycles, indicated by points B and C. Considering now a smaller value of $\delta_{\nu 1}$, as shown by the results in Fig. 4(b), there is no significant degradation in moment capacity at points A and B, whereas there is a significant degradation from points B to C, such that the degradation has been effectively delayed by the smaller value of $\delta_{\nu 1}$. Fig. 4(c) also shows that the parameter $\delta_{\nu 1}$ affects the shape of the degradation curve and hence by reducing the value of $\delta_{\nu 1}$ from 1 to 0.01, curvature/convexity of the curve is changed, resulting in negligible initial degradation in the region OA. As such, the commonly observed degradation phenomenon is observed, when the degradation only starts after a few hysteretic cycles and then grows thereafter.

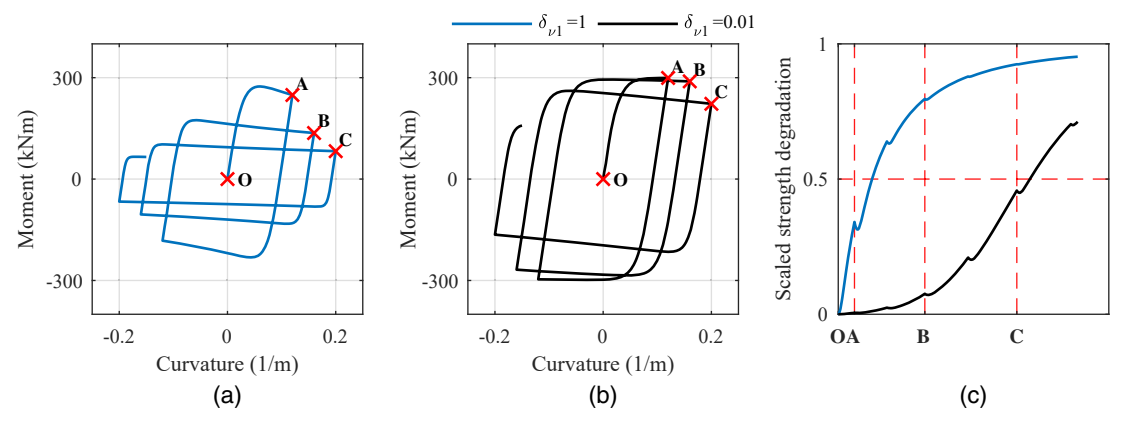


Fig. 4. Effect of parameter $\delta_{\nu 1}$ for constant $\delta_{\nu 2}=1.5\times 10^{-5}$ and $\delta_{\nu 3}=0$, resulting in different initial degradations.

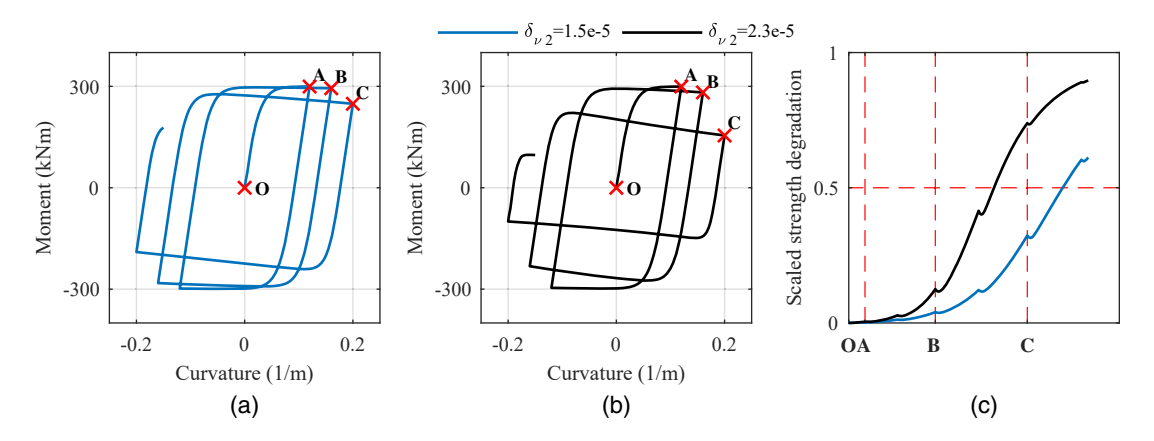


Fig. 5. Effect of parameter $\delta_{\nu 2}$ for constant $\delta_{\nu 1}=0.005$ and $\delta_{\nu 3}=0$, altering degradation evolution.

Next, the effect of parameter $\delta_{\nu 2}$ is illustrated in Fig. 5, in which the value of $\delta_{\nu 1}=0.005$ is used for all simulations. The moment-curvature response for $\delta_{\nu 2}=1.5\times 10^{-5}$ and $\delta_{\nu 2}=2.3\times 10^{-5}$ is plotted in Figs. 5(a and b), respectively. As can be observed, increasing the value of $\delta_{\nu 2}$ from 1.5×10^{-5} in Fig. 5(a) to 2.3×10^{-5} in Fig. 5(b) results in an increase in the rate of degradation in the consecutive cycles. Again, consistent response is evident from Fig. 5(c), presenting same initial degradations but different degradation growth rates for the given $\delta_{\nu 2}$ values.

Strain-Based Component

The effect of the parameter $\delta_{\nu 3}$ is illustrated by setting $\delta_{\nu 2}=0$ in Eq. (4), thus resulting in Eq. (9):

$$\nu_{\phi} = 1 + \delta_{\nu 1} [((\varepsilon_{\phi} - \varepsilon_{\phi_{\text{neak}}}) \text{sgn}(\Delta \varepsilon_{\phi}) + 1)^{\delta_{\nu 3}} - 1]$$
 (9)

Eq. (9) is formulated such that the strength degradation now is directly proportional to the absolute value of $(\varepsilon_{\phi} - \varepsilon_{\phi_{\rm peak}})$, where the absolute value is ensured by multiplying the term with ${\rm sgn}(\Delta\varepsilon_{\phi})$. Furthermore, the value of degradation function in Eq. (9) is equal to 1 for the localized peak curvature values, i.e., $\varepsilon_{\phi} = \varepsilon_{\phi_{\rm peak}}$, and increases as the value of ε_{ϕ} moves further away from $\varepsilon_{\phi_{\rm peak}}$, for both reloading and unloading branches. Therefore, in the elastic region, when $\varepsilon_{\phi} \approx \varepsilon_{\phi_{\rm peak}}$, degradation is negligible, while in the inelastic part, large degradation function values can be obtained. The parameter $\delta_{\nu 3}$ is used to further intensify the effect of degradation with

respect to the change in curvature values. Again, the parameter $\delta_{\nu 1}$ scales the overall degradation effect.

To illustrate this concept graphically, Fig. 6(a) shows two single moment-curvature hysteretic cycles, where both nondegrading and degrading cycles are generated with Eqs. (1) and (9), and Fig. 6(b) shows their corresponding scaled degradation functions based on Eq. (3). In the reloading branch of the hysteretic loop, given by RST, $\varepsilon_{\phi_{\text{peak}}}$ corresponds to the value of curvature at point R, i.e., $\varepsilon_{\phi_{\mathrm{peak}}} = \varepsilon_{\phi(R)}$. Therefore, both $\Delta \varepsilon_{\phi} > 0$ and $(\varepsilon_{\phi} - \varepsilon_{\phi_{\mathrm{peak}}}) \geq 0$ result in positive and increasing values of $(\varepsilon_{\phi} - \varepsilon_{\phi_{\text{peak}}}) \operatorname{sgn}(\Delta \varepsilon_{\phi})$ for every point in the branch RST. Also, $(\varepsilon_\phi-\varepsilon_{\phi_{\rm peak}})\approx 0$ in the elastic region of RS, which according to Eq. (9) produces $\nu_{\phi} \approx 1$, and therefore there is no degradation in the elastic region. In contrast, large values as well as a continuous increase in $(\varepsilon_{\phi} - \varepsilon_{\phi_{\text{peak}}})$ values from point S to point T, result in large and increasing strength degradation values in the plastic region, enhancing the so-called softening effect. Moreover, initial degradation at point S can be further reduced by selecting a small value of parameter $\delta_{\nu 1}$, similar to the energy dissipation effect described earlier, and the strain-based effect can be magnified by increasing the parameter value $\delta_{\nu 3}$, resulting in relative increase of the degradations at point T as compared to point S. As for the unloading region PQR, $\varepsilon_{\phi_{\text{neak}}}$ corresponds to the value of curvature at point P. Hence, the curvature values are continuously decreasing in the region PQR, i.e., $\Delta \varepsilon_{\phi} < 0$ and $(\varepsilon_{\phi} - \varepsilon_{\phi_{\text{peak}}}) \le 0$, again resulting in positive and increasing values of $(\varepsilon_{\phi} - \varepsilon_{\phi_{\text{peak}}}) \text{sgn}(\Delta \varepsilon_{\phi})$ for all the points along

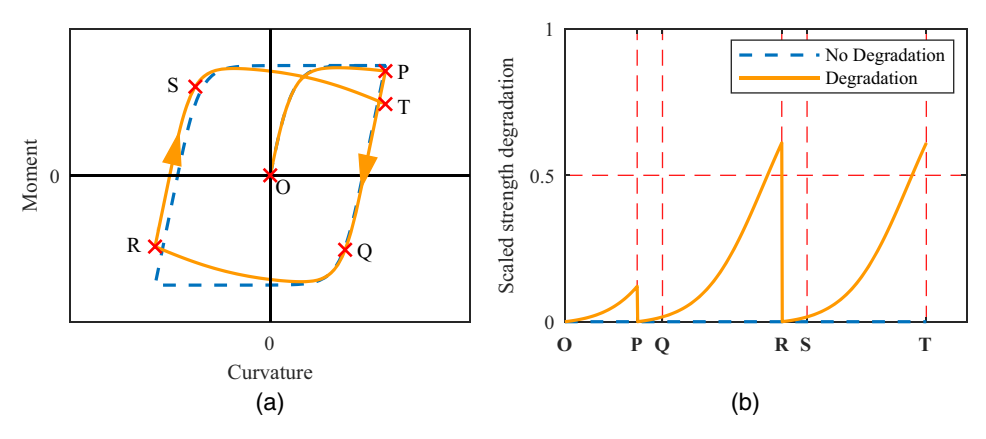


Fig. 6. Strain-based degradation evolution.

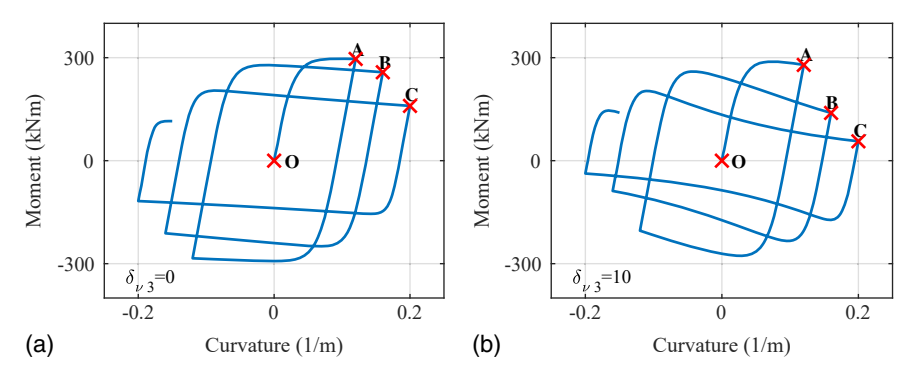


Fig. 7. Effect of strength degradation parameter $\delta_{\nu 3}$, for constant $\delta_{\nu 1}=0.05$ and $\delta_{\nu 2}=1.5\times 10^{-5}$.

this segment. Therefore, similar to the reloading branch, the value of ν_{ϕ} is approximately 1 at point Q, and increases to a maximum value at point R, where the $\varepsilon_{\phi_{\mathrm{peak}}}$ value again changes and the process repeats similarly for all the subsequent cycles.

The effect of the parameter $\delta_{\nu 3}$ is graphically illustrated in Fig. 7 using Eqs. (1) and (4) with constant values of $\delta_{\nu 1}=0.05$ and $\delta_{\nu 2}=1.5\times 10^{-5}$. It can be seen that by increasing the value of $\delta_{\nu 3}$ from 0 in Fig. 7(a) to 10 in Fig. 7(b), the softening effect is enhanced.

Summarizing, scaling parameter $\delta_{\nu 1}$ primarily affects the onset of degradation, such that for $\delta_{\nu 1}=0$ there is no strength degradation, parameter $\delta_{\nu 2}$ controls the effect of cumulative energy dissipation allowing nonuniformly degrading hysteretic loops, and $\delta_{\nu 3}$ is the strain-based parameter, directly controlling the softening effects in the element. Hence, based on different values of parameters $\delta_{\nu 1},\delta_{\nu 2}$, and $\delta_{\nu 3}$, versatile physically observed strength degradation phenomena can be obtained.

Integration with Stiffness Degradation and Pinching Functions

In this section, the newly proposed strength degradation function is integrated with other degradation functions to collectively simulate a large range of degrading behaviors. As such, the following stiffness degradation function (Baber and Wen 1981; Baber and Noori 1985) is adopted:

$$\eta_{\phi} = 1 + \delta_{\eta} e_{\phi} \tag{10}$$

where parameter δ_{η} controls the degree of stiffness degradation. Setting the parameter value equal to zero results in no stiffness

degradation, whereas varying degrees of stiffness degradation can be achieved by setting the value of δ_η greater than zero.

To simulate pinching related phenomena, an existing pinching function is next adopted and simplified to reduce its number of parameters while retaining the fidelity of the original formulation. For the benefit of the subsequent discussion, the pinching function proposed by Foliente (1995) is reproduced here:

$$h_{\phi} = 1 - \zeta_{1\phi} \exp\left(-\left(\frac{z_{\phi} \operatorname{sgn}(\dot{\varepsilon}_{\phi}) - q z_{\phi}^{u}}{\zeta_{2\phi}}\right)^{2}\right)$$

$$z_{\phi}^{u} = \left(\frac{1}{\nu_{\phi}(\beta + \gamma)}\right)^{1/n} \tag{11}$$

where functions $\zeta_{1\phi}=\zeta_{10}(1-\exp(-pe_\phi))$ and $\zeta_{2\phi}=(\psi_0+\delta_\psi e_\phi)$ ($\lambda+\zeta_{1\phi}$) control the degree of pinching and width of the pinching region, respectively; and ζ_{10} , p, q, ψ_0 , δ_ψ , and λ are the time invariant parameters. In an effort to reduce the number of parameters and ensure compatibility with the proposed formulation, the expression in Eq. (11) is now modified. The effect of $\zeta_{2\phi}$ can be achieved through a combination of the stiffness degradation parameter, δ_η , and a subset of the pinching parameters, and therefore it can be simplified from a functional form to a constant parameter ζ_{20} . The simplified pinching function is now given as:

$$h_{\phi} = 1 - \zeta_{1\phi} \exp\left(-\left(\frac{(M^h/|M_c^h|)\operatorname{sgn}(\Delta\varepsilon_{\phi}) - q}{\zeta_{20}}\right)^2\right)$$

$$\zeta_{1\phi} = \zeta_{10}(1 - \exp(-pe_{\phi})) \tag{12}$$

where ζ_{10} , ζ_{20} , p, and q are the pinching parameters. Specifying the value of ζ_{10} to be zero results in no pinching. Similar to the original

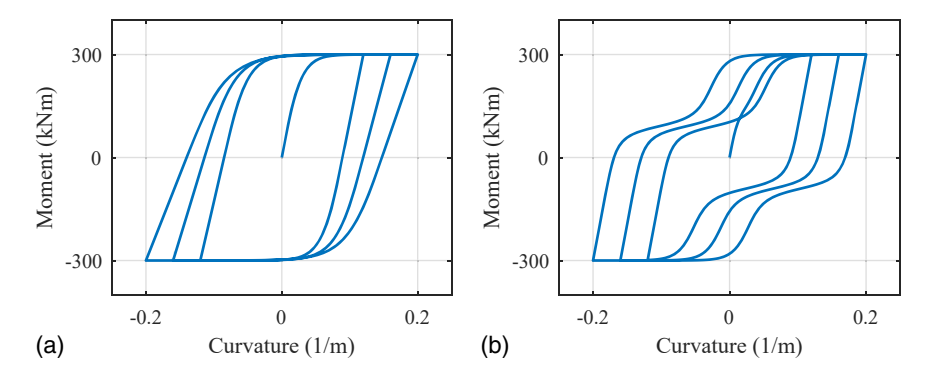


Fig. 8. (a) Stiffness degradation; and (b) pinching phenomena.

function, parameter p controls the rate of initial slope reduction, ζ_{10} controls the total slip, q sets a fraction of M_c^h as the pinching level, and ζ_{20} is a normalizing factor that causes the pinching region to grow. The pinching function adopted here is presented in terms of hysteretic moment in Eq. (12), instead of hysteretic curvature in Eq. (11), to be compatible with the present evolution equation in Eq. (1). Additionally, for further simplification, pinching is assumed to occur when the hysteretic bending moment, M^h , is q times the initial nondegrading capacity, M_c^h , for all the hysteretic cycles. Therefore, with $(\beta+\gamma)=1$, and without considering any strength degradation, the z_ϕ^u term can be eliminated, ensuring that the pinching occurs when $|M^h/M_c^h|=q$ and $\mathrm{sgn}(M^h\Delta\varepsilon_\phi)=1$.

Illustrative results for stiffness degradation and pinching are shown in Fig. 8. The simulated response shown in Fig. 8(a) is obtained by combining Eqs. (1) and (10) to illustrate stiffness degradation with parameter value $\delta_{\eta}=3\times 10^{-6}$, and Fig. 8(b) shows pinching behavior obtained by combining Eqs. (1) and (12) with pinching parameter values $\zeta_{10}=0.95$, $\zeta_{20}=0.34$, $p=8\times 10^{-4}$, and q=0.3.

Asymmetric Hysteresis

In the case of asymmetric cross sections, different yield capacities in compression and tension can be accounted for in the degrading hysteretic model using the following expression for M_c^h (Wang et al. 2001):

$$M_c^h = c(M^h)M_c^{h+} + c(-M^h)M_c^{h-}$$
 (13)

where M_c^{h-} and M_c^{h+} are the section capacities in compression and tension respectively, and the Heaviside function $c(\cdot)$ is defined in Eq. (6). Furthermore, asymmetric responses in the hysteresis can also be obtained for all the degradation functions. For asymmetric stiffness degradation, i.e., different rates of degradation for reloading and unloading cycles, the following stiffness degradation function can be adopted:

$$\eta_{\phi} = c(\Delta \varepsilon_{\phi}) \eta_{\phi}^{+} + c(-\Delta \varepsilon_{\phi}) \eta_{\phi}^{-}$$
 (14)

where $\eta_\phi^+=1+\delta_\eta^+e_\phi$ and $\eta_\phi^-=1+\delta_\eta^-e_\phi$ are the stiffness degradation functions corresponding to reloading and unloading cycles respectively, defined by different parameter values. For symmetric stiffness degradation, same parameters are obtained for both reloading and unloading cycles, resulting in $\eta_\phi^+=\eta_\phi^-=\eta_\phi$. Next, for simulating asymmetry in the strength degradation, the following function is employed:

$$\nu_{\phi} = c(M^h)\nu_{\phi}^+ + c(-M^h)\nu_{\phi}^- \tag{15}$$

where ν_{ϕ}^{+} and ν_{ϕ}^{-} are the strength degradation functions corresponding to tension and compression respectively, again defined by their corresponding parameter values. Similarly, the pinching function is defined as:

$$h_{\phi} = c(\Delta \varepsilon_{\phi}) h_{\phi}^{+} + c(-\Delta \varepsilon_{\phi}) h_{\phi}^{-}$$
 (16)

where h_{ϕ}^{+} and h_{ϕ}^{-} are the pinching functions corresponding to reloading and unloading branches, respectively.

Illustrative results for asymmetry in stiffness degradation, strength degradation, and pinching are shown in Fig. 9, by using the required asymmetry based on Eqs. (13)-(16) and then substituting Eqs. (4), (10), and (12) into Eq. (1), while applying the appropriate parameter values. The parameter values in Fig. 9(a) for asymmetric stiffness degradation are $\delta_{\eta}^{+} = 3.6 \times 10^{-6}$ and $\delta_{\eta}^{-}=1.5\times 10^{-6}$; in Fig. 9(b) for asymmetric strength degradation are $\delta^+_{\nu 1}=0.01,~\delta^-_{\nu 1}=1,~\delta_{\nu 2}=1.5\times 10^{-5},~{\rm and}~\delta_{\nu 3}=0;~{\rm and}~{\rm in}$ Fig. 9(c) for asymmetric pinching are $\zeta^+_{10}=0.96,~\zeta^-_{10}=0.90,$ $\zeta_{20} = 0.34$, $p = 8 \times 10^{-4}$, and q = 0.3. As such, a wide variety of hysteretic behaviors can be simulated, as illustrated by the results presented in Fig. 10, where Fig. 10(a) shows combined strength and stiffness degradations with $\delta_{\eta} = 3.0 \times 10^{-6}$, $\delta_{\nu 1} = 0.005$, $\delta_{\nu 2} =$ 2.0×10^{-5} , and $\delta_{\nu 3} = 1$, in Fig. 10(b) asymmetric yielding is added with $M_c^{h+} = 300$ kNm and $M_c^{h-} = 200$ kNm, and Fig. 10(c) shows the result of combining all the described degradations by also employing nonzero pinching parameters values $\zeta_{10} = 0.95$, $\zeta_{20} =$ 0.34, $p = 8 \times 10^{-4}$, and q = 0.3.

Multiaxial Hysteretic Laws/Hysteretic Evolution Equations

Consistent with Eq. (1), the generalized hysteretic laws at any distance x along a beam element of length L are expressed as:

$$N_{(x)} = N_{(x)}^{e} + N_{(x)}^{h} = \alpha_{u} E A \varepsilon_{u(x)} + (1 - \alpha_{u}) E A z_{u(x)}$$

$$Q_{(x)} = Q_{(x)}^{e} + Q_{(x)}^{h} = \alpha_{\gamma} G A_{s} \varepsilon_{\gamma(x)} + (1 - \alpha_{\gamma}) G A_{s} z_{\gamma(x)}$$

$$M_{(x)} = M_{(x)}^{e} + M_{(x)}^{h} = \alpha_{\phi} E I \varepsilon_{\phi(x)} + (1 - \alpha_{\phi}) E I z_{\phi(x)}$$
(17)

where $N_{(x)}$, $Q_{(x)}$, and $M_{(x)}$ are the axial force, shear force, and bending moment, respectively; and superscripts e and h correspond to the respective elastic and hysteretic components; A is the cross section area; A_s is the effective shear area; G is the shear modulus; and α_u and α_γ are the axial and shear hardening

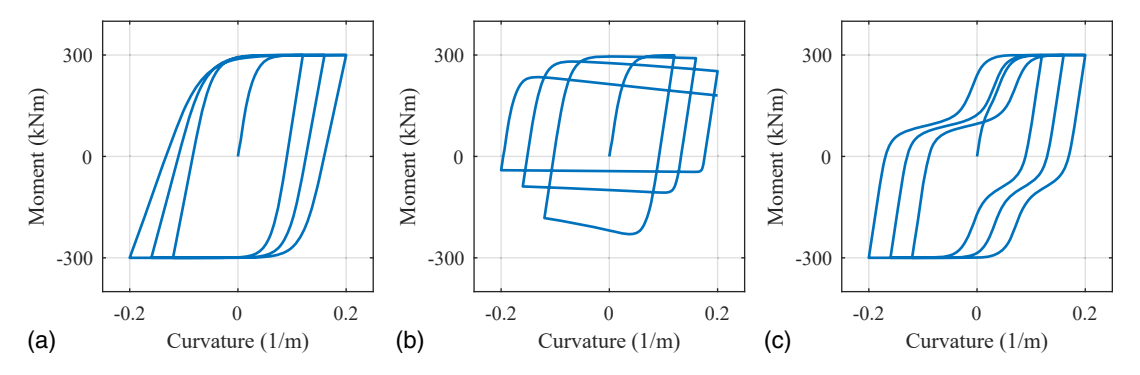


Fig. 9. (a) Asymmetric stiffness degradation; (b) asymmetric strength degradation; and (c) asymmetric pinching.

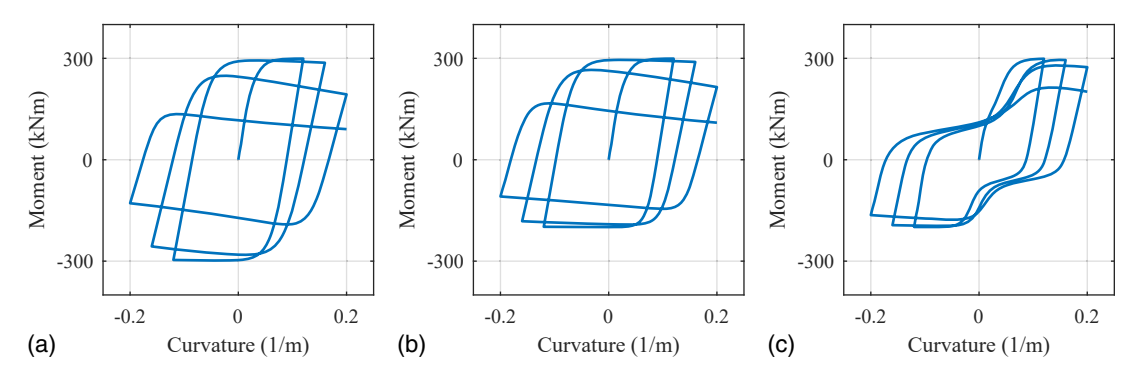


Fig. 10. (a) Strength and stiffness degradations; (b) asymmetric yielding, strength, and stiffness degradations; and (c) combined pinching, asymmetric yielding, strength, and stiffness degradations.

parameters, respectively. Eq. (17) is further expressed in vectorized form as:

$$\mathbf{P}_{(x)} = \mathbf{P}_{(x)}^{e} + \mathbf{P}_{(x)}^{h} = \alpha \mathbf{D} \boldsymbol{\varepsilon}_{(x)} + (\mathbf{I} - \alpha) \mathbf{D} \mathbf{z}_{(x)}$$
(18)

$$\mathbf{P}_{(x)} = \begin{cases} N \\ Q \\ M \end{cases}; \quad \boldsymbol{\varepsilon}_{(x)} = \begin{cases} \varepsilon_{u} \\ \varepsilon_{\gamma} \\ \varepsilon_{\phi} \end{cases}; \quad \mathbf{z}_{(x)} = \begin{cases} z_{u} \\ z_{\gamma} \\ z_{\phi} \end{cases}_{(x)}$$
$$\mathbf{D} = \begin{bmatrix} EA \\ GA_{s} \\ EI \end{bmatrix} \quad \boldsymbol{\alpha} = \begin{bmatrix} \alpha_{u} \\ \alpha_{\gamma} \\ \alpha_{\phi} \end{bmatrix}$$
(19)

where $\mathbf{P}^e_{(x)}$ and $\mathbf{P}^h_{(x)}$ are the elastic and hysteretic components of $\mathbf{P}_{(x)}$, respectively; $\boldsymbol{\varepsilon}_{(x)}$ and $\mathbf{z}_{(x)}$ are the strain and hysteretic deformation vectors, respectively; $\boldsymbol{\alpha}$ is the strain hardening matrix; \mathbf{D} is the rigidity matrix; and \mathbf{I} is the identity matrix. The hysteretic deformation vector, $\mathbf{z}_{(x)}$, is described using evolution equations, that can be formulated to account for a variety of modeling assumptions, ranging from no-interaction/degradation to coupled degradation-plasticity, as described in the subsequent subsections, starting with the most basic case.

Case 1: No Degradations and No Interactions

For the simplest case, when the degradations and capacity interactions are not considered, the hysteretic moment-curvature relation can be expressed as:

$$\dot{M}_{(x)}^{h} = (1 - \alpha_{\phi})EI\left(1 - \left|\frac{M^{h}}{M_{c}^{h}}\right|^{n} (\beta + \gamma \operatorname{sgn}(M^{h}\dot{\varepsilon}_{\phi}))\right)\dot{\varepsilon}_{\phi(x)}$$
(20)

Similar equations are also available for axial force-axial strain, N^h - ε_u , and shear force-shear strain, Q^h - ε_γ , that have been omitted for brevity. With $M^h=(1-\alpha_\phi)EIz_\phi$, Eq. (20) can be expressed in terms of the hysteretic curvature evolution as shown below:

$$\dot{z}_{\phi(x)} = \left(1 - \left|\frac{M^h}{M_c^h}\right|^n (\beta + \gamma \operatorname{sgn}(M^h(\varepsilon_{\phi} - \varepsilon_{\phi 0})))\right) \dot{\varepsilon}_{\phi(x)} \tag{21}$$

Note that Eq. (21) is similar to Eq. (1) with $h_{\phi} = \nu_{\phi} = \eta_{\phi} = 1$, but with a slight modification in sgn(.) function. For numerical implementation purposes in quasi-static problems, it is assumed that $\mathrm{sgn}(M^h\dot{\varepsilon}_{\phi}) \approx \mathrm{sgn}(M^h(\varepsilon_{\phi} - \varepsilon_{\phi_0}))$, where ε_{ϕ_0} is the initial strain at the beginning of each solution step, as previously defined. With all the degradation functions equal to 1 for this case, degradation effects are not considered, and due to the assumption of no capacity interactions, all the hysteretic deformations evolve independently based on their full capacities.

Case 2: Degradations with No Capacity Interactions

Another possible model is to assume the system under consideration degrades, but the capacity interactions are neglected. In other words, axial force, bending moment and shear force are assumed to evolve and degrade based on their independent capacities, strains and energy dissipations. For this case, the moment-curvature expression is formulated as:

$$\dot{M}_{(x)}^{h} = (1 - \alpha_{\phi})EI\frac{h_{\phi}}{\eta_{\phi}} \left(1 - \nu_{\phi} \left| \frac{M^{h}}{M_{c}^{h}} \right|^{n} (\beta + \gamma \operatorname{sgn}(M^{h} \dot{\varepsilon}_{\phi})) \right) \dot{\varepsilon}_{\phi(x)}$$
(22)

As such, the hysteretic curvature evolution for this case is given by:

$$\dot{z}_{\phi(x)} = \frac{h_{\phi}}{\eta_{\phi}} \left(1 - \nu_{\phi} \left| \frac{M^{h}}{M_{c}^{h}} \right|^{n} (\beta + \gamma \operatorname{sgn}(M^{h}(\varepsilon_{\phi} - \varepsilon_{\phi 0}))) \right) \dot{\varepsilon}_{\phi(x)}$$
 (23)

In essence, Eq. (23) is adopting the uniaxial degrading hysteretic model, as obtained in Eq. (1), for moment-curvature, shear force-shear strain, and axial force-axial strain mapping, resulting in an overall multiaxial degrading hysteretic model without interactions. Importantly, Eq. (23) presents a general form for no interaction case, comprising both Cases 1 and 2, because the evolution equation shown in Eq. (23) reverts to Eq. (21) by specifying appropriate degradation parameter values.

Case 3: Capacity Interactions with No Degradations

For the previous two cases, the axial force, moment, and shear force have been assumed to evolve following their respective independent uniaxial hysteretic laws/models, such that the individual capacities are not constrained by any multiaxial yield/capacity surface. If needed, the evolution laws can be modified to incorporate axial-moment-shear interactions (Sivaselvan and Reinhorn 2004; Triantafyllou and Koumousis 2011a; Amir et al. 2020) using the following:

$$\dot{\mathbf{P}}_{(x)}^{h} = \mathbf{H}_{\mathbf{D}}(\mathbf{I} - H_1 H_2 \mathbf{R}) \dot{\boldsymbol{\varepsilon}}_{(x)}; \quad \text{where } \mathbf{P}^{h} = \{N^{h} Q^{h} M^{h}\}^{T} \quad (24)$$

$$H_{1} = |\Phi(\mathbf{P}^{h}) + 1|^{n}; \qquad H_{2} = \beta + \gamma \operatorname{sgn}((\mathbf{P}^{h})^{T} \dot{\boldsymbol{e}});$$

$$\mathbf{R} = \left[\left(\frac{\partial \Phi}{\partial \mathbf{P}^{h}} \right)^{T} \mathbf{D} \left(\frac{\partial \Phi}{\partial \mathbf{P}^{h}} \right) \right]^{-1} \left[\left(\frac{\partial \Phi}{\partial \mathbf{P}^{h}} \right) \left(\frac{\partial \Phi}{\partial \mathbf{P}^{h}} \right)^{T} \mathbf{D} \right]$$
(25)

where $\mathbf{H_D} = (\mathbf{I} - \boldsymbol{\alpha})\mathbf{D}$ is the hysteretic rigidity matrix; H_1 is a smooth function ranging in [0,1] corresponding to the elastic and plastic regions, respectively; H_2 is a Heaviside function; and $\Phi(\mathbf{P}^h)$ is the specified yield/capacity function. Note, Eq. (24) is derived based on classical plasticity theory satisfying the Kuhn-Tucker optimality conditions (Sivaselvan and Reinhorn 2004) (see Appendix II for detailed derivations related to this fact). With $\mathbf{P}_{(x)}^h = \mathbf{H_D}\mathbf{z}_{(x)}$, the multiaxial hysteretic evolution equation can be obtained as:

$$\dot{\mathbf{z}}_{(r)} = (\mathbf{I} - H_1 H_2 \mathbf{R}) \dot{\boldsymbol{\varepsilon}}_{(r)} \tag{26}$$

where function H_1 and matrix **R** are obtained using Eq. (25). However, for quasistatic problems, it is necessary to approximate H_2 as $H_2 \approx \beta + \gamma \text{sgn}((\mathbf{P}^h)^T(\boldsymbol{\varepsilon} - \boldsymbol{\varepsilon}_0))$.

Case 4: Coupled Degradation-Plasticity

Case 3 represents a smooth hysteretic model with full axial-moment-shear interactions following classical plasticity theory without degradations. In Case 2, the uniaxial model is simply extended to capture various degradation effects; however, axial-moment-shear interactions are not considered. Here, the most general case is addressed, of how to incorporate degradations while satisfying the consistency condition of the yield/capacity surface following the classical multiaxial plasticity theory. As such, a consistent hysteretic degradation-plasticity model is proposed here where both degradations and multiaxial yield/capacity surface

interactions are evolving in a consistent framework. The stiffness and pinching functions, affecting only the elastic loading and unloading regions, do not alter the capacity surface, and thus, they can be implemented similar to Case 2. However, strength degradation functions are evolving with time to reduce the section capacities. Therefore, treating these in the same manner as for the uniaxial case violates the Kuhn-Tucker consistency criterion of the capacity surface. In order to satisfy the capacity surface consistency condition, the strength degradation is considered here using the effective stress and strain hypothesis. Accordingly, the effective hysteretic bending moment is defined as:

$$\bar{M}^h = \frac{M^h}{1 - d_\phi} \tag{27}$$

where d_ϕ is the scalar damage function corresponding to the flexure capacity, such that $d_\phi \in [0\,1)$ ranging from intact/undamaged to fully damaged state. The coefficient of $(1-d_\phi)$ in the denominator of Eq. (27) is a reduction factor associated with the amount of damage in the material (Kachanov 1980), analogous to degradation in this case. Based on the range of the damage function, it can be defined same as the scaled strength degradation function described earlier in Eq. (3), and again specified as:

$$d_{\phi} = 1 - \frac{1}{\nu_{\phi}} \quad \text{or} \quad \nu_{\phi} = \frac{1}{1 - d_{\phi}} \quad \text{where,} \quad \begin{array}{c} \nu_{\phi} \in [1 \quad \infty) \\ d_{\phi} \in [0 \quad 1) \end{array}$$
 (28)

For multiaxial plasticity, based on different strength degradation functions corresponding to each action, different scalar damage functions are defined, resulting in the following effective hysteretic force vector:

$$\bar{\mathbf{P}}^{h} = \begin{cases}
\bar{N}^{h} \\
\bar{Q}^{h} \\
\bar{M}^{h}
\end{cases} = \begin{cases}
N^{h}/(1 - d_{u}) \\
Q^{h}/(1 - d_{\gamma}) \\
M^{h}/(1 - d_{\phi})
\end{cases} = \begin{cases}
\nu_{u}N^{h} \\
\nu_{\gamma}Q^{h} \\
\nu_{\phi}M^{h}
\end{cases}$$

$$= \begin{bmatrix}
\nu_{u} \\
\nu_{\gamma} \\
\nu_{\phi}M^{h}
\end{bmatrix} = \mathbf{P}^{h}$$

$$\nu_{\phi} \begin{bmatrix}
N^{h} \\
Q^{h} \\
M^{h}
\end{bmatrix} = \mathbf{P}^{h}$$
(29)

where d_u and d_γ are the scalar damage functions corresponding to axial strength degradation, ν_u , and shear strength degradation, ν_γ , respectively. Additionally, hypothesis of strain equivalence states that the strain associated with a damaged state under the applied stress is equivalent to the strain associated with its undamaged state under the effective stress (Lemaitre 1996). Therefore, based on Eq. (24), the multiaxial hysteretic model/laws for the damaged material can be expressed in the effective stress domain, considering no damage, as:

$$\dot{\bar{\mathbf{P}}}_{(x)}^{h} = \mathbf{H}_{\mathbf{D}}(\mathbf{I} - \bar{H}_{1}\bar{H}_{2}\bar{\mathbf{R}})\dot{\boldsymbol{\varepsilon}}_{(x)}$$
(30)

where \bar{H}_1 , \bar{H}_2 , and $\bar{\mathbf{R}}$ are the functions of the hypothetical effective hysteretic force, $\bar{\mathbf{P}}^h$, and true strain, $\boldsymbol{\varepsilon}$, given by:

$$\bar{\boldsymbol{H}}_{1} = |\Phi(\bar{\mathbf{P}}^{h}) + 1|^{n}; \qquad \bar{\boldsymbol{H}}_{2} = \beta + \gamma \operatorname{sgn}((\bar{\mathbf{P}}^{h})^{T} \hat{\boldsymbol{\varepsilon}});
\bar{\mathbf{R}} = \left[\left(\frac{\partial \Phi}{\partial \bar{\mathbf{P}}^{h}} \right)^{T} \mathbf{D} \left(\frac{\partial \Phi}{\partial \bar{\mathbf{P}}^{h}} \right) \right]^{-1} \left[\left(\frac{\partial \Phi}{\partial \bar{\mathbf{P}}^{h}} \right) \left(\frac{\partial \Phi}{\partial \bar{\mathbf{P}}^{h}} \right)^{T} \mathbf{D} \right]$$
(31)

Eqs. (30) and (31), similar to Eq. (24), as also shown in Appendix II, satisfy the multiaxial classical plasticity theory postulates, adhering to the consistency of the capacity surface, i.e., $\dot{\Phi}(\bar{\bf P}^h)=0$. Now, by employing Eq. (29), Eq. (30) can be

expressed in terms of the true hysteretic force and generalized strains as

$$\dot{\mathbf{P}}_{(x)}^{h} = \boldsymbol{\nu}^{-1} [\mathbf{H}_{\mathbf{D}} (\mathbf{I} - \bar{H}_{1} \bar{H}_{2} \mathbf{\bar{R}}) \dot{\boldsymbol{\varepsilon}}_{(x)} - \dot{\boldsymbol{\nu}} \mathbf{P}_{(x)}^{h}]$$
(32)

As already mentioned, pinching function and stiffness degradation affect only the elastic part of the hysteresis, and thus they can be introduced here similar to Case 2, resulting in the following equation:

$$\dot{\mathbf{P}}_{(x)}^{h} = \mathbf{h} \boldsymbol{\eta}^{-1} \boldsymbol{\nu}^{-1} [\mathbf{H}_{\mathbf{D}} (\mathbf{I} - \bar{H}_{1} \bar{H}_{2} \mathbf{\tilde{R}}) \dot{\boldsymbol{\varepsilon}}_{(x)} - \dot{\boldsymbol{\nu}} \mathbf{P}_{(x)}^{h}]$$
where $\mathbf{h} = \begin{bmatrix} h_{u} \\ h_{\gamma} \\ h_{\phi} \end{bmatrix}$; $\boldsymbol{\eta} = \begin{bmatrix} \eta_{u} \\ \eta_{\gamma} \\ \eta_{\phi} \end{bmatrix}$ (33)

Eq. (33) represents the final multiaxial hysteretic model, expressed in terms of axial force, shear force, and moment, and their corresponding strains, i.e., centerline axial strain, shear strain, and curvature. Since the model satisfies the plasticity postulates, a consistent evolution of the capacity surface with degradations is now obtained. Eq. (33) is treated as a consistent constitutive law for the hysteretic finite-element formulation herein; however, it can be readily adopted for other modeling approaches, e.g., in fiber elements (Spacone et al. 1996; Scott et al. 2008; Andriotis et al. 2018) to represent stress-strain relationships and model cross section behaviors, among many other applications. Because $\mathbf{P}_{(x)}^h = \mathbf{H}_{\mathbf{D}}\mathbf{z}_{(x)}$, the hysteretic deformation vector is obtained as:

$$\dot{\mathbf{z}}_{(x)} = \mathbf{h} \boldsymbol{\eta}^{-1} \boldsymbol{\nu}^{-1} [(\mathbf{I} - \bar{H}_1 \bar{H}_2 \bar{\mathbf{R}}) \dot{\boldsymbol{\varepsilon}}_{(x)} - \dot{\boldsymbol{\nu}} \mathbf{z}_{(x)}]$$
 (34)

Eq. (34) presents the proposed multiaxial hysteretic yield/capacity evolution with degradation effects. In Eq. (34), strength degradation is introduced through ν , pinching through \mathbf{h} , and stiffness degradation is obtained by the combination of ν and η . For $\nu = \mathbf{h} = \eta = \mathbf{I}$, Eq. (34) reverts to Eq. (26), that corresponds to the multiaxial interaction case with no degradation. Therefore, Eq. (34) presents a general multiaxial interaction case, applicable for both Cases 3 and 4. In the subsequent section, a consistent degrading hysteretic finite-element formulation is proposed based on the described multiaxial hysteretic evolution equations.

Degrading Hysteretic Beam Finite Element Formulation

A parametrized hysteretic beam finite-element model has been derived in Amir et al. (2020), using consistent two-node Timoshenko elements, to efficiently simulate the nonlinear behavior of structural systems. Here a similar approach is used to derive a degrading hysteretic beam finite-element model with the suggested multiaxial hysteretic evolution equations. However, for the benefit of the subsequent discussion, first the essential aspects of the element in Amir et al. (2020) are reviewed. In this beam element, six additional degrees of freedom (DOF) are required to account for hysteretic axial, bending, and shear deformations for each element. Hence, the nodal displacement and hysteretic DOF vectors are expressed as:

$$\mathbf{d} = \{u_1 w_1 \theta_1 u_2 w_2 \theta_2\}^T; \quad \mathbf{z} = \{z_{u1} z_{\gamma 1} z_{\phi 1} z_{u2} z_{\gamma 2} z_{\phi 2}\}^T \quad (35)$$

where **d** is the nodal displacement vector in local coordinates, consisting of longitudinal displacement u, transverse displacement w, and rotation θ ; **z** represents the six additional hysteretic DOF, consisting of hysteretic axial deformation z_u , shear deformation z_γ , and

bending deformation z_{ϕ} , which are set to evolve through ODEs; and the subscripts 1 and 2 correspond to the start and end nodes of the element. The following compatibility interpolation functions for $\mathbf{z}_{(x)} = \{z_{u(x)} \, z_{\gamma(x)} \, z_{\phi(x)}\}^T$ are used to account for distributed plasticity over the length of the element:

$$z_{u(x)} = \left(\frac{1}{2}\right) z_{u1} + \left(\frac{1}{2}\right) z_{u2}; \qquad z_{\gamma(x)} = \left(\frac{1}{2}\right) z_{\gamma 1} + \left(\frac{1}{2}\right) z_{\gamma 2}$$

$$z_{\phi(x)} = \left(1 - \frac{x}{L}\right) z_{\phi 1} + \left(\frac{x}{L}\right) z_{\phi 2}$$
(36)

Original displacement and rotation interpolation functions have been derived that satisfy both the exact equilibrium and kinematic conditions of the nonlinear Timoshenko beam element but have been omitted here for brevity [see Amir et al. (2020) for details]. Based on the derived interpolation functions, the strain-displacement expressions for the beam element is obtained as:

$$\boldsymbol{\varepsilon}_{(x)} = \mathbf{B}_{(x)}\mathbf{d} + \mathbf{H}_{\mathbf{B}(x)}\mathbf{z} \tag{37}$$

where $\mathbf{B}_{(x)}$ and $\mathbf{H}_{\mathbf{B}(x)}$ are the linear and hysteretic strain matrices, respectively (see Appendix I for details). Using the suggested interpolation functions, strain-displacement relation, and the nodal boundary conditions, the following force-displacement relation is derived for the beam element:

$$\mathbf{F} = \mathbf{Kd} + \mathbf{Hz} \tag{38}$$

where **F** is the element nodal force vector; **K** and **H** are the constant element stiffness and hysteretic matrices, respectively (see Appendix I for details), that do not require updating throughout the analysis.

Based on the multiaxial degrading hysteretic models/laws described in the previous section, and the consistent displacement, rotation, and hysteretic deformation interpolation functions, derived in Amir et al. (2020), a degrading hysteretic beam finite-element model is proposed here. Since the degradations and multiaxial plasticity are incorporated through the hysteretic DOFs, which are set to evolve through the suggested ODEs, the constant element matrices of Appendix I are still preserved in the present formulation. For the detailed derivation of element matrices, refer to Amir et al. (2020).

The formulation can be conveniently presented in state-space form for dynamic cases, similar to Triantafyllou and Koumousis (2011a, b), and be efficiently solved using appropriate ODE solver, avoiding any type of linearizations. In quasi-static problems, however, the solution process is not as straightforward due to the presence of algebraic equations now, in addition to the ODEs, resulting in a set of complex and hard to solve differential algebraic equations (DAEs). Yet, an efficient solution scheme for such problems is presented in this paper, where instead of DAEs only a set of ODEs are again required to be solved, similar to the dynamic cases. Through the suggested approach, the number of unknowns to be updated at each pseudotime step of the resulting ODEs are also significantly reduced, in comparison to both DAE systems and the typically used Newton's method, reducing computational complexity and increasing efficiency even further.

The subsequent subsections, categorized into three parts, describe a method to integrate the degradations and multiaxial plasticity in a hysteretic finite-element framework at the system level, and present a computationally efficient solution scheme that does not require linearization to solve the resulting system of equations for quasi-static problems. More specifically, in the first part, the

force-displacement expression is obtained in terms of system stiffness and hysteretic matrices, and their corresponding DOFs. The second part presents the evolution equations for the system hysteretic DOFs based on the four cases described in the previous section, and lastly the third part describes the numerical solution scheme.

System Force-Displacement Expression

The vectors and matrices in Eq. (38) correspond to local element coordinates. The typical transformation matrix is used to transform Eq. (38) to the global coordinates as (Bathe 1996):

$$\mathbf{F}_{g} = \mathbf{K}_{g}\mathbf{d}_{g} + \mathbf{H}_{g}\mathbf{z}; \text{ where } \mathbf{K}_{g} = \mathbf{\Lambda}^{T}\mathbf{K}\mathbf{\Lambda}; \qquad \mathbf{H}_{g} = \mathbf{\Lambda}^{T}\mathbf{H};$$

$$\mathbf{d} = \mathbf{\Lambda}\mathbf{d}_{g}; \qquad \mathbf{F}_{g} = \mathbf{\Lambda}^{T}\mathbf{F}$$
(39)

 Λ is the standard coordinate transformation matrix; and \mathbf{F}_g and \mathbf{d}_g correspond to the element nodal force and displacement DOF vectors in global coordinates, respectively. Also, \mathbf{K}_g and \mathbf{H}_g are the element stiffness and hysteretic matrices in global coordinates, respectively. The former is then mapped to the symmetric system stiffness matrix, by the typical direct stiffness matrix assembly techniques (Bathe 1996), and the latter forms the system hysteretic matrix, by consistently appending the \mathbf{H}_g matrices for all the elements (Amir et al. 2020). The overall system force-displacement expression, after applying appropriate displacement boundary conditions, is thus expressed as:

$$\mathbf{F}_{s} = \mathbf{K}_{s} \mathbf{d}_{s} + \mathbf{H}_{s} \mathbf{z}_{s} \quad \text{where } \mathbf{z}_{s} = \begin{cases} \mathbf{z}_{(el=1)} \\ \vdots \\ \mathbf{z}_{(el=N_{el})} \end{cases}$$
(40)

 \mathbf{K}_s is the symmetric and positive definite system stiffness matrix; \mathbf{H}_s is the resulting system hysteretic matrix; \mathbf{F}_s and \mathbf{d}_s are the system nodal force and displacement DOF vectors, respectively; $\mathbf{z}_{(el=j)}$ is the hysteretic DOF vector of dimensions 6×1 for the jth element $(j = \{1, 2, \dots, N_{el}\})$, where N_{el} is the total number of elements in the system; and \mathbf{z}_s is the vector consisting of the hysteretic DOF for all the elements.

System Evolution Equations

Additional equations in the form of evolution equations for \mathbf{z}_s are required to augment the system of equations presented in Eq. (40) in order to solve for the unknown DOFs. This subsection describes the form of the evolution equations for the various modeling assumptions outlined in Case 1 through Case 4 of the previous section. As can be seen in the first three cases of the multiaxial hysteretic models/laws, i.e., in Eqs. (21), (23), and (26), the rate of change of the hysteretic deformation vector at a distance x, i.e., $\dot{\mathbf{z}}_{(x)}$, is a nonlinear function of $(\nu, \eta, \mathbf{h}, \mathbf{P}^h, \boldsymbol{\varepsilon})_{(x)}$ and linearly dependent on $\dot{\boldsymbol{\varepsilon}}_{(x)}$. The degradation functions $(\boldsymbol{\nu}, \boldsymbol{\eta}, \mathbf{h})_{(x)}$ can be further expressed in terms of $(\mathbf{e}^h, \mathbf{P}^h, \boldsymbol{\varepsilon})_{(x)}$, following Eqs. (4), (10), and (12), where $\mathbf{e}^h = \{e_u \, e_{\gamma} \, e_{\phi}\}^T$. In other words, for Cases 1–3, $\dot{\mathbf{z}}_{(x)}$ can be expressed as a nonlinear function of $(\mathbf{e}^h, \mathbf{P}^h, \boldsymbol{\varepsilon})_{(x)}$ multiplied to $\dot{\boldsymbol{\varepsilon}}_{(x)}$. However, for Case 4, the derivative of the strength degradation function is also required, as indicated by Eq. (34), that can be obtained using the chain rule, leading to the expression:

$$\dot{\nu}_{\phi} = \frac{\partial \nu(e_{\phi}, \varepsilon_{\phi})}{\partial e_{\phi}} \dot{e}_{\phi} + \frac{\partial \nu(e_{\phi}, \varepsilon_{\phi})}{\partial \varepsilon_{\phi}} \dot{\varepsilon}_{\phi}
= \left(\frac{\partial \nu(e_{\phi}, \varepsilon_{\phi})}{\partial e_{\phi}} M^{h} + \frac{\partial \nu(e_{\phi}, \varepsilon_{\phi})}{\partial \varepsilon_{\phi}}\right) \dot{\varepsilon}_{\phi}; \quad \text{where } \dot{e}_{\phi} = M^{h} \dot{\varepsilon}_{\phi}$$
(41)

The derivatives of ν_u and ν_γ are similarly obtained. Substituting Eq. (41) into Eq. (34), the evolution equation for Case 4 can also be expressed in the form shown in Eq. (42), similar to Cases 1–3.

$$\dot{\mathbf{z}}_{(x)} = \mathbf{f}_c(\mathbf{e}_{(x)}^h, \mathbf{P}_{(x)}^h, \boldsymbol{\varepsilon}_{(x)}) \dot{\boldsymbol{\varepsilon}}_{(x)}; \text{ where}$$

$$\mathbf{e}^h = \{e_u \, e_\gamma \, e_\phi\}^T \tag{42}$$

and \mathbf{f}_c represents different functional forms depending on Cases 1 through 4, as indicated by the subscript $c = \{1, 2, 3, 4\}$. Now, applying the boundary conditions at the start (x = 0) and end nodes $(x = L_j)$ of the jth beam element, the nodal hysteretic DOFs for all the cases can be expressed as:

$$\dot{\mathbf{z}}_{(el=j)} = \begin{bmatrix} \mathbf{f}_c(\mathbf{e}^h, \, \mathbf{P}^h, \, \boldsymbol{\varepsilon})_{(x=0)} & \mathbf{0} \\ \mathbf{0} & \mathbf{f}_c(\mathbf{e}^h, \, \mathbf{P}^h, \boldsymbol{\varepsilon})_{(x=L_j)} \end{bmatrix} \dot{\boldsymbol{\varepsilon}}_{(el=j)};$$

where
$$\dot{\mathbf{z}}_{(el=j)} = \{z_{u1} \ z_{\gamma 1} \ z_{\phi 1} \ z_{u2} \ z_{\gamma 2} \ z_{\phi 1}\}_{(el=j)}^{T};$$

$$\boldsymbol{\varepsilon}_{(el=j)} = \{\varepsilon_{u1} \ \varepsilon_{\gamma 1} \ \varepsilon_{\phi 1} \ \varepsilon_{u2} \ \varepsilon_{\gamma 2} \ \varepsilon_{\phi 2}\}_{(el=j)}^{T}$$

$$(43)$$

In Eq. (43), the hysteretic energy dissipation is approximated as $\mathbf{e}_{(x)}^h \approx \mathbf{e}_{0(x)}^h + \mathbf{P}_{(x)}^h(\boldsymbol{\varepsilon}_{(x)} - \boldsymbol{\varepsilon}_{0(x)})$, where $\mathbf{e}_{0(x)}^h$ is the initial hysteretic energy at the beginning of a step. Therefore, $\dot{\boldsymbol{z}}_{(el=j)}$ in Eq. (43) becomes a function of \mathbf{P}^h , $\boldsymbol{\varepsilon}$, and $\dot{\boldsymbol{\varepsilon}}$. By expressing \mathbf{P}^h at x=0 and $x=L_j$ in terms of hysteretic DOF and employing the strain-displacement relation shown in Eq. (37), Eq. (43) can be now compactly expressed as:

$$\dot{\mathbf{z}}_{(el=j)} = \mathbf{g}_c(\mathbf{d}_{(el=j)}, \mathbf{z}_{(el=j)})\dot{\mathbf{d}}_{(el=j)}$$
(44)

where $\mathbf{d}_{(el=j)} = (\Lambda \mathbf{d}_g)_{(el=j)} = (\Lambda \mathbf{L}_d)_{(el=j)} \mathbf{d}_s$ and $\mathbf{z}_{(el=j)} = \mathbf{L}_{z(el=j)} \mathbf{z}_s$, such that \mathbf{L}_d and \mathbf{L}_z are the incidence (or connectivity) matrices that transform vectors \mathbf{d}_g and \mathbf{z} for each element to the global system vectors \mathbf{d}_s and \mathbf{z}_s , respectively, and \mathbf{g}_c is a new functional mapping resulting from the transformation of Eq. (43) to Eq. (44). The elements in the incidence matrices are 1, corresponding to the same DOF in both row and column, and 0 otherwise (Bathe 1996).

Solution Scheme

For a given external force vector, the system force-displacement Eq. (40) and the evolution equation in Eq. (44) have to be solved simultaneously to obtain the unknown DOFs, which results in a system of DAEs, where Eq. (40) is a set of algebraic equations, while Eq. (44) is a set of first order differential equations. The DAEs from Eqs. (40) and (44) can be solved for the unknown nodal displacements, \mathbf{d}_s , and hysteretic DOF, \mathbf{z}_s , at each step, using a Newton scheme by approximating the ODE in Eq. (44) in an algebraic form.

Alternatively, the system of DAEs can be modified so as to be conducive to the use of more efficient ODE solution schemes, for example Runge-Kutta methods (RKMs). To facilitate the ODE solution scheme, the displacement expression from Eq. (40) is substituted into the evolution equation of Eq. (44), so the resulting

expression forms an explicit first order ODE system with respect to the vector \mathbf{z}_s . Specifically, the system of ODEs is obtained by first re-expressing Eq. (40) to the following form:

$$\mathbf{d}_{s} = \mathbf{K}_{s}^{-1} \mathbf{F}_{s} - \mathbf{K}_{s}^{-1} \mathbf{H}_{s} \mathbf{z}_{s} \tag{45}$$

From Eq. (44), the overall evolution equation for the system is expressed as:

$$\dot{\mathbf{z}}_{s} = \begin{bmatrix} \mathbf{g}_{c(el=1)} & & & \\ & \ddots & & \\ & & \mathbf{g}_{c(el=N_{el})} \end{bmatrix} \begin{bmatrix} (\mathbf{\Lambda} \mathbf{L}_{\mathbf{d}})_{(el=1)} \\ & \vdots \\ (\mathbf{\Lambda} \mathbf{L}_{\mathbf{d}})_{(el=N_{el})} \end{bmatrix} \dot{\mathbf{d}}_{s} = \mathbf{g}_{s}(\mathbf{d}_{s}, \mathbf{z}_{s}) \dot{\mathbf{d}}_{s}$$

$$(46)$$

By substituting the expression for \mathbf{d}_s from Eq. (45) into Eq. (46), the following evolution equation is obtained:

$$\dot{\mathbf{z}}_s = (\mathbf{I} + \mathbf{g}_s \mathbf{K}_s^{-1} \mathbf{H}_s)^{-1} \mathbf{g}_s \mathbf{K}_s^{-1} \dot{\mathbf{F}}_s$$
 (47)

where \mathbf{K}_s and \mathbf{H}_s are the previously defined constant system matrices, and from Eqs. (45) and (46), \mathbf{g}_s becomes a function of the unknown \mathbf{z}_s vector. Thus, the only equations needed to solve the problem are the ODEs in Eq. (47), which inherently represent a form of model reduction, since the displacement DOF have been eliminated from the evolution equation without any loss of fidelity and accuracy. Hence, the present hysteretic finite-element model with the suggested numerical solution scheme transforms the entire system into a first order system of ODEs, obtained in Eq. (47), which enables the use of any common numerical ODE solver, e.g., the family of RKMs, for obtaining the hysteretic DOFs. With \mathbf{z}_s at each time step, the nodal displacements, \mathbf{d}_s , can be simply obtained from Eq. (45), either through post processing or through a separate concurrent step in the analysis. For all numerical results described in the subsequent sections, Eq. (47) with an appropriate RKM solver has been used.

Note that due to its parametrized nature, the present degrading hysteretic beam finite-element model can be used for both Timoshenko and Euler-Bernoulli beam formulations, with linear/ nonlinear, degrading/nondegrading behaviors, or any combination thereof. For example, for the pure elastic Timoshenko case with no degradations, the hardening parameters are $\alpha_u = \alpha_\gamma = \alpha_\phi = 1$, so that the hysteretic matrix in Appendix I becomes null, and degradation parameters, i.e., $\delta_{\eta},\,\delta_{\nu 1},$ and $\zeta_{10},$ in the evolution equations are set to zero. Alternatively, for $\lambda=0$ and $\alpha_{\gamma}=1$, the matrices in Appendix I transform to inelastic Euler-Bernoulli formulation, thus resulting in a degrading hysteretic Euler-Bernoulli beam element. Another simplified form could be a nondegrading elastic Euler-Bernoulli beam element, obtained by combining the aforementioned cases, i.e., $\lambda = 0$, $\alpha_u = \alpha_{\gamma} = \alpha_{\phi} = 1$, $\delta_n = \delta_{\nu 1} = \zeta_{10} = 0$. It is also important to note that although different formulations can be obtained from the suggested most generalized form by changing the values of a few parameters, the present model in its most general form can be also employed to accurately identify the response of structural systems without a priori knowledge of the associated element behavior, such as linear/nonlinear, flexure dominant or shear dominant phenomena.

Illustrative Results

To illustrate the consistency, versatility, and generality of the suggested degrading hysteretic beam finite-element model, a set of

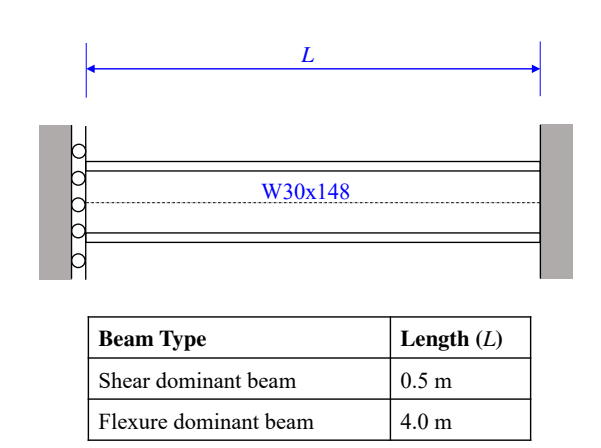


Fig. 11. Beam element for illustrative examples.

numerical simulations are conducted on pertinent beam elements, related to the four distinct cases: Case 1 with no degradations and no interactions; Case 2 exhibiting degradations without capacity interactions; Case 3 with no degradations but having capacity interactions; and lastly Case 4 presenting the fully coupled degradation-plasticity model with interactions. For each case, two beam models are considered, as shown in Fig. 11, having identical properties other than their overall lengths. The first beam model has a specified length of 0.5 m, showcasing significant shear deformation, and hence is referred to here as shear dominant beam. The second beam model analyzed is a flexure dominant beam with a longer length of 4.0 m, such that the beam deformation is predominantly due to flexure. For both beam models, the DOFs at their end nodes are assumed to be fully restrained, except for the transverse displacement at one end, where the beam is subjected to a displacement based cyclic loading protocol with increasing amplitude, used in all numerical analysis cases in this section.

Both shear and flexure dominant models are based on a $W30 \times 148$ steel beam, with web yield strength of 450 MPa, flange yield strength of 380 MPa, elastic modulus of 200 GPa, and shear modulus of 77 GPa. The model parameters based on the beam mechanical properties are accordingly obtained as: E = 200 GPa, G = 77 GPa, $N_p = 11,450 \text{ kN}$, $Q_p = 3,300 \text{ kN}$, and $M_p =$ 3,200 kNm; and the parameters derived from the cross sectional properties are: $A = 280 \text{ cm}^2$, $A_s = 128 \text{ cm}^2$, and $I = 278,040 \text{ cm}^4$. Other hysteretic parameters assumed are: n = 1 for smooth transition from elastic to plastic regime; $\beta = \gamma = 0.5$ resulting in unloading stiffness equal to the loading stiffness; $\alpha_u = \alpha_\phi = \alpha_\gamma = 0$, assuming no kinematic hardening; $\delta_{\eta}=\zeta_{10}=0$, resulting in no stiffness degradation and pinching from Eqs. (10) and (12); and $\delta_{\nu 1}=0.01,\,\delta_{\nu 2}=3\times 10^{-6},$ and $\delta_{\nu 3}=2$ for strength degradation, given by Eq. (4). For Cases 3 and 4, considering full interaction between axial, shear and bending, the following generalized Gendy-Saleeb capacity surface criterion is considered (Gendy and Saleeb 1993):

$$\Phi(\mathbf{P}^h) = n_u^2 + q_\gamma^2 + \frac{1}{\lambda_u} m_\phi^2 - 1$$
 (48)

where $n_u=N^h/N_c^h$, $q_\gamma=Q^h/Q_c^h$, $m_\phi=M^h/M_c^h$, and $\lambda_u=1-1.1|n_u|$ for wide flange I-cross sections.

All results are summarized in Fig. 12 in a tabular form, where the rows represent the presented four distinct cases, described earlier. In Fig. 12, plots (a-b) presented in the first two columns, are

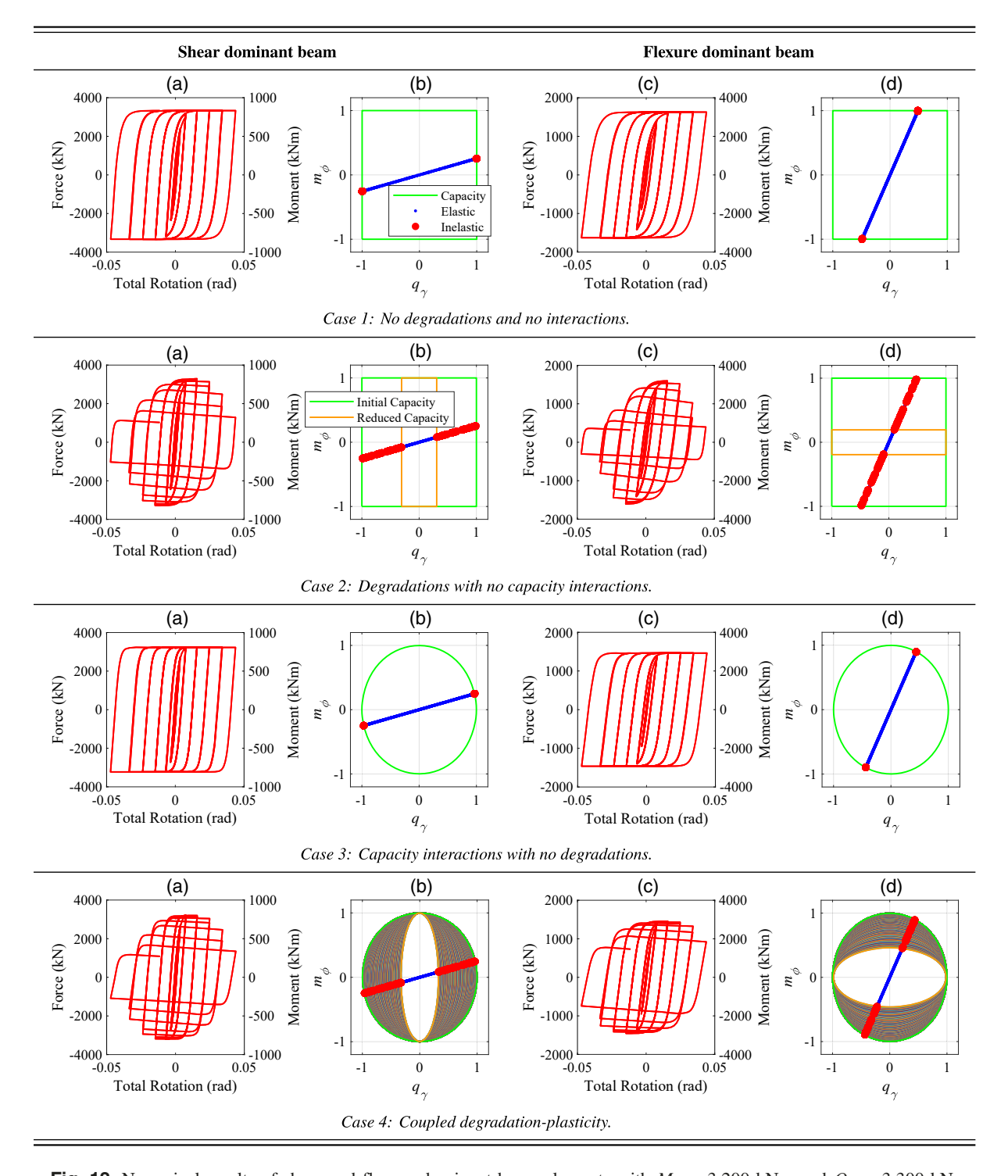


Fig. 12. Numerical results of shear and flexure dominant beam elements with $M_p = 3,200$ kNm and $Q_p = 3,300$ kN.

the global hysteretic response and moment-shear interactions, respectively, for each modeling case of the shear dominant beam. Similarly, plots (c-d) in the last two columns are the hysteretic response and moment-shear interaction, respectively, for the flexure dominant beam. For the hysteretic response in plots (a) and (c), the left and right y-axes correspond to the shear force and moment, respectively, whereas the x-axis shows the total beam rotation, obtained by normalizing the displacement at the free end with respect to the beam length. In the interaction plots (b) and (d), blue dots indicate the normalized moment-shear values at each analysis step,

red dots give the same values when the hysteretic capacity is reached, and green line/curve presents the initial maximum capacity that can be reached by a nondegrading system, whereas orange line/curve corresponds to the final reduced section capacities (color figure can be viewed online).

Case 1: No degradations and No Interactions

The first row of Fig. 12 presents this case. For the shear dominant beam, in plots (a) and (b), it can be seen that the shear capacity of

the beam, i.e., $Q_p=3,300$ kN, is reached, indicating inelastic shear deformations, while the bending moment remains in the elastic range, i.e., $M < M_p = 3,200$ kNm. As can be seen in plot (b), there are no interactions between the moment-shear capacities, and thus there is no capacity reduction. However, due to the required moment-shear equilibrium, i.e., 2M=QL, there is a linear normalized moment (m_ϕ) -shear (q_γ) mapping, indicated by the linear alignment of the blue dots, that also limits the maximum moment based on the shear capacity. Similarly, for the flexure dominant beam, shown in plots (c) and (d), the bending capacity is reached, while the corresponding shear force is well below its capacity. Plot (d) again shows that the equilibrium is satisfied, indicated by the straight blue line as before, that now has a larger slope in comparison to the shear beam, due to increased beam length, limiting the maximum shear force based on the bending capacity.

Summarizing this case, plots (a–b) appropriately demonstrate that the beam response is governed by shear deformations and shear capacities, while plots (c–d) show that the beam response is dominated by the flexural properties, and for both shear and flexure beam models, equilibrium is exactly satisfied.

Case 2: Degradations with No Capacity Interactions

The case of strength degradation with no capacity interactions is shown in the second row of Fig. 12, wherein the first few hysteretic cycles are similar to Case 1. However, in contrast to Case 1, after the onset of degradation, the shear capacity in plots (a-b) is degrading based on the hysteretic shear energy dissipation and shear deformations, while there is no degradation in the flexural capacity of the beam due to negligible flexural deformations, as indicated by the constant capacity in the y-direction (normalized moment axis) of plot (b). In other words, the response of the shear dominant beam with degradation is solely governed by shear deformation, shear capacity, and shear energy dissipation. Similarly, for the flexure dominant beam, the degradations are occurring due to significant flexural deformations and cumulative flexural energy dissipation. Again, similar to Case 1, although the moment-shear capacities are not interacting, they are inter-dependent on each other due to the equilibrium conditions satisfied in a strong sense everywhere through the force-displacement expression of Eq. (40), resulting in the observed blue straight line, as explained before.

As previously mentioned, Case 2 is a general case, when the capacities interactions are not considered in the system, and can be transformed to Case 1, by simply selecting the degradation parameters $\delta_{\nu 1}=\delta_{\eta}=\zeta_{10}=0$.

Case 3: Capacity Interactions with No Degradations

As shown in the third row of Fig. 12, there is moment-shear interaction in this case, without degradation effects, as shown by the circular surface and its constant amplitude in plots (b) and (d). Similar to Case 1, the maximum force/moment for the shear dominant beam corresponds to the shear capacity of the beam, while the maximum plastic limit in the flexure dominant beam accords to the bending capacity. However, the plastic capacities in both beams are reduced now as compared to Case 1, based on the plots (b) and (d) in the third row, showing the interaction surface of Eq. (48), that is here rewritten, given that the axial force is absent, as:

$$\Phi(\mathbf{P}^h) = q_{\gamma}^2 + m_{\phi}^2 - 1 = 0 \tag{49}$$

The same effect of slight reduction in the maximum capacities, based on the interaction surface, can be seen in plots (a) and (c), as compared to Case 1. Hence, Eq. (49) represents a circular

capacity surface, restricting the maximum values of moment and shear force, as shown in plots (b) and (d).

In summary, Case 3 satisfies in a fully consistent manner, both the equilibrium conditions and capacity interaction criteria, for shear and flexure dominant beams.

Case 4: Coupled Degradation-Plasticity

Results for the case of coupled degradation-plasticity, indicating interactions with strength degradation, is presented in the fourth row of Fig. 12. Similar to Case 3, the first few cycles of the hysteretic loops again reach their nondegrading interacting capacities based on the shear and flexure dominant responses of the beam elements, indicating interactions but no degradations in the initial cycles. For this case, the capacity surface is now obtained as:

$$\Phi(\bar{\mathbf{P}}^h) = \bar{q}_{\gamma}^2 + \bar{m}_{\phi}^2 - 1 = (\nu_{\gamma}q_{\gamma})^2 + (\nu_{\phi}m_{\phi})^2 - 1 = 0$$
 (50)

When $\nu_{\gamma} = \nu_{\phi} \approx 1$, i.e., before the onset of degradation, the maximum plastic capacity is constrained by the constant amplitude circular surface, as indicated by the green circle in plots (b) and (d). After the degradation initiates, the value of ν_{γ} increases continuously for the shear dominant beam, due to large shear deformation and shear energy dissipation, whereas $\nu_{\phi} \approx 1$ due to small flexural deformation, with both functions having the same parameter values. Therefore, to appropriately satisfy the capacity surface criteria of Eq. (50), q_{γ} decreases while m_{ϕ} almost remains constant, as indicated by the contraction of capacity surface in the x-direction (normalized shear axis). Again, the blue line followed by (m_{ϕ}, q_{γ}) satisfies the beam equilibrium and the red dots present the updated evolving plastic limits consistent with yield/capacity surface criteria. In this case, the evolution of yield/capacity surfaces are also indicated, for more clarity, starting from the initial constant amplitude green surface to the final degraded orange one. Similarly, for the flexure dominant beam, m_{ϕ} decreases while q_{γ} remains stationary to satisfy Eq. (50), resulting in the contraction of the interaction capacity surface in the y-direction (normalized moment axis).

In summary, Case 4 consistently incorporates capacity interactions and degradations, while satisfying exact equilibrium conditions at all points. This most general modeling case can also be used to simulate the response of Case 3, by simply choosing values of the degradation parameters as $\delta_{\nu 1} = \delta_{\eta} = \zeta_{10} = 0$.

Experimental Verifications

The previous section validates that the proposed model is compatible with theoretical assumptions and intuitive knowledge. To further verify the capability of the model to replicate physical observations, simulated responses are compared with the available experimental test results. Three examples are presented, based on the experimental setups shown in Figs. 13 and 14, with each one exhibiting varied combinations of degradation phenomena, to showcase the versatility of the modeling approach, and the results are summarized in Fig. 15. For all three reported experiments, the simulation is done using both the linear-rate strength degradation and the new strength degradation functions, the former shown in the first column, and the latter presented in the second column. Full axial-shear-bending interaction is considered using the Gendy-Saleeb capacity surface criterion (Gendy and Saleeb 1993), as shown in Eq. (48), and the hysteretic finite-element formulation with fully coupled degradation-plasticity phenomenon described in Case 4 is used for all the experimental results.

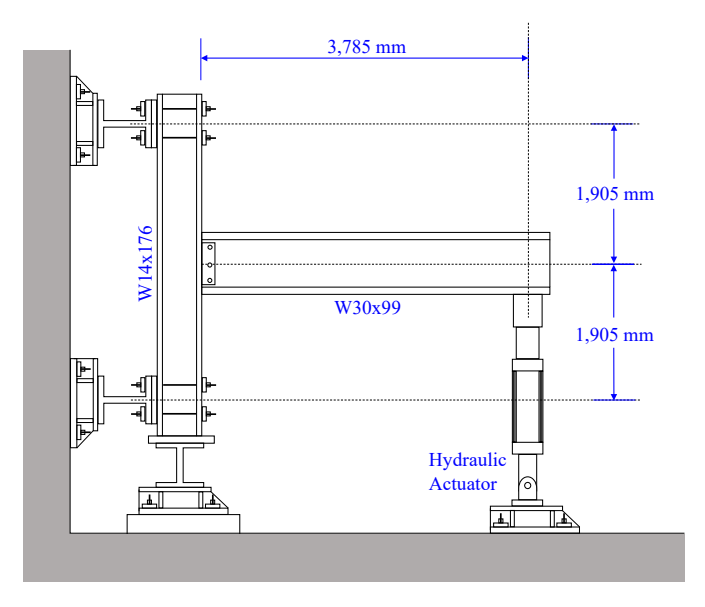


Fig. 13. Experimental setup for beam-column moment connection.

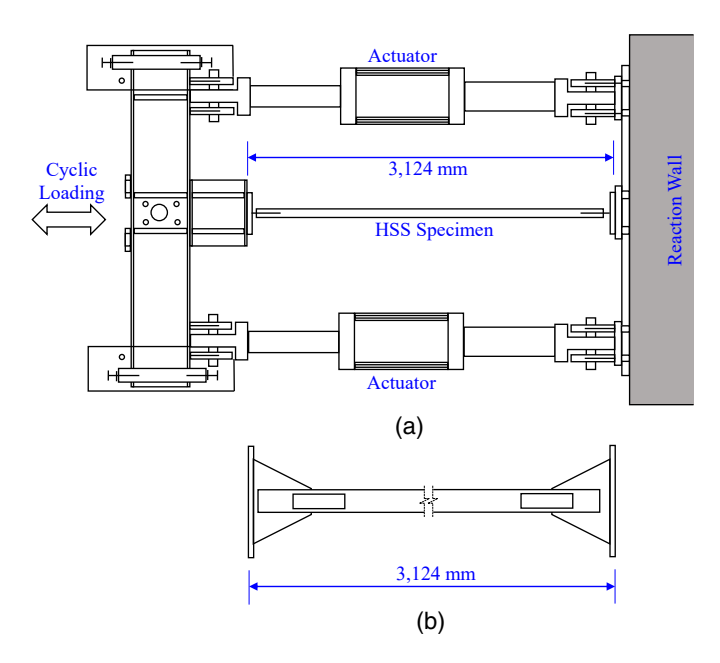


Fig. 14. Experimental setup for buckling brace: (a) plan view of the setup; and (b) HSS specimen.

Example 1: Reduced Beam Section (RBS) Moment Connection with Deep Wide Flange Column

The *first row* of Fig. 15 presents the analysis of a RBS moment connection with deep wide flange column, where the simulated responses are compared to the experimental data from Yu et al. (2000). In this example, specimen LS-1 from Yu et al. (2000) is selected, exhibiting significant strength degradation. The specimen, as shown in Fig. 13, consists of a W14 \times 176 column, with web yield strength of 375 MPa and flange yield strength of 386 MPa; and a W30 \times 99 beam, with web and flange yield strengths of 400 and 377 MPa, respectively. The beam length from the loading point to the centerline of the column is 3.8 m, while the column length to the centerline of the beam is 1.9 m. The column ends

are fully restrained, while the free end of the beam is subjected to a standard displacement based SAC loading protocol (Clark et al. 1997). Further details about the experimental setup, cross sectional geometry, loading history, etc., can be seen in Yu et al. (2000).

For the suggested degrading hysteretic finite-element formulation, the beam is modeled as one element, while the column is discretized into two elements, with a node at the beam-column connection. The parameters of the beam and column elements are tabulated in Tables 1–3, where the mechanical and geometrical parameters are obtained based on the material and the cross sectional properties of the elements. The hysteretic parameters are obtained using a sequential quadratic programming (SQP) optimization algorithm, by minimizing the sum of the squared error between the experimental data and the simulated responses for all inelastic cycles, for both linear-rate and new strength degradation functions. Note that same hysteretic parameters are assumed here for all the elements; however, the hardening and degradation parameters are not activated for the column elements, because their deformations remain in the elastic range.

The results of the developed degrading hysteretic finiteelement formulation with linear-rate and new strength degradation functions are shown in plots (a) and (b), respectively, of the first row in Fig. 15. It can be seen in plot (a) that the simulated response is not able to accurately simulate the full capacity of the section in the first few inelastic cycles, because the initial capacity is also reduced in order to capture the later inelastic cycles, which are also not very effectively captured in this case. Note that if the degradation parameter value increases to replicate the last cycle, it will also decrease the initial capacity. On the other hand, if the parameter value decreases to capture the initial capacity, the plastic limit of the last simulated cycle will be much higher than the experimental one. Therefore, the relevant parameter in the linear-rate function is trying to simulate the degrading response based on the uniform degradation evolution constraints. Yet, in plot (b), it is apparent that the simulated degradation evolution is almost identical to the experimental one, and all the capacity cycles are captured with better accuracy as compared to the linearrate ones.

Example 2: Weak Axis RBS Beam-Column Moment Connection

To simulate the cyclic response of a weak axis RBS moment connection, experimental data for specimen CW-1 (Gilton and Uang 2002) are employed here. The experimental setup is similar to Fig. 13; however, it consists of a W14 \times 398 column, with a yield strength of 386 MPa, and a W36 \times 150 beam, with web and flange yield strengths of 359 and 400 MPa, respectively. The beam length from the loading point to the centerline of the column is 3.6 m, while the column length to the centerline of the beam is 1.9 m. In this case, one end of the beam is connected to the column web, such that the column is bending about its weak axis, and the other end is subjected to the SAC loading protocol (Clark et al. 1997), similar to Example 1. The parameters are again tabulated in Tables 4–6.

Results are presented in the *second row* of Fig. 15, demonstrating a combination of significant strength and stiffness degradation. The linear-rate degradation formulation, as shown in plot (a) of the second row, is not able to simulate very well the strength and stiffness degradations in the later unloading and reloading cycles. On the contrary, plot (b) with the proposed strength degradation function is aptly replicating the experimental behavior until the very last cycle. For all the hysteretic cycles, the transition from

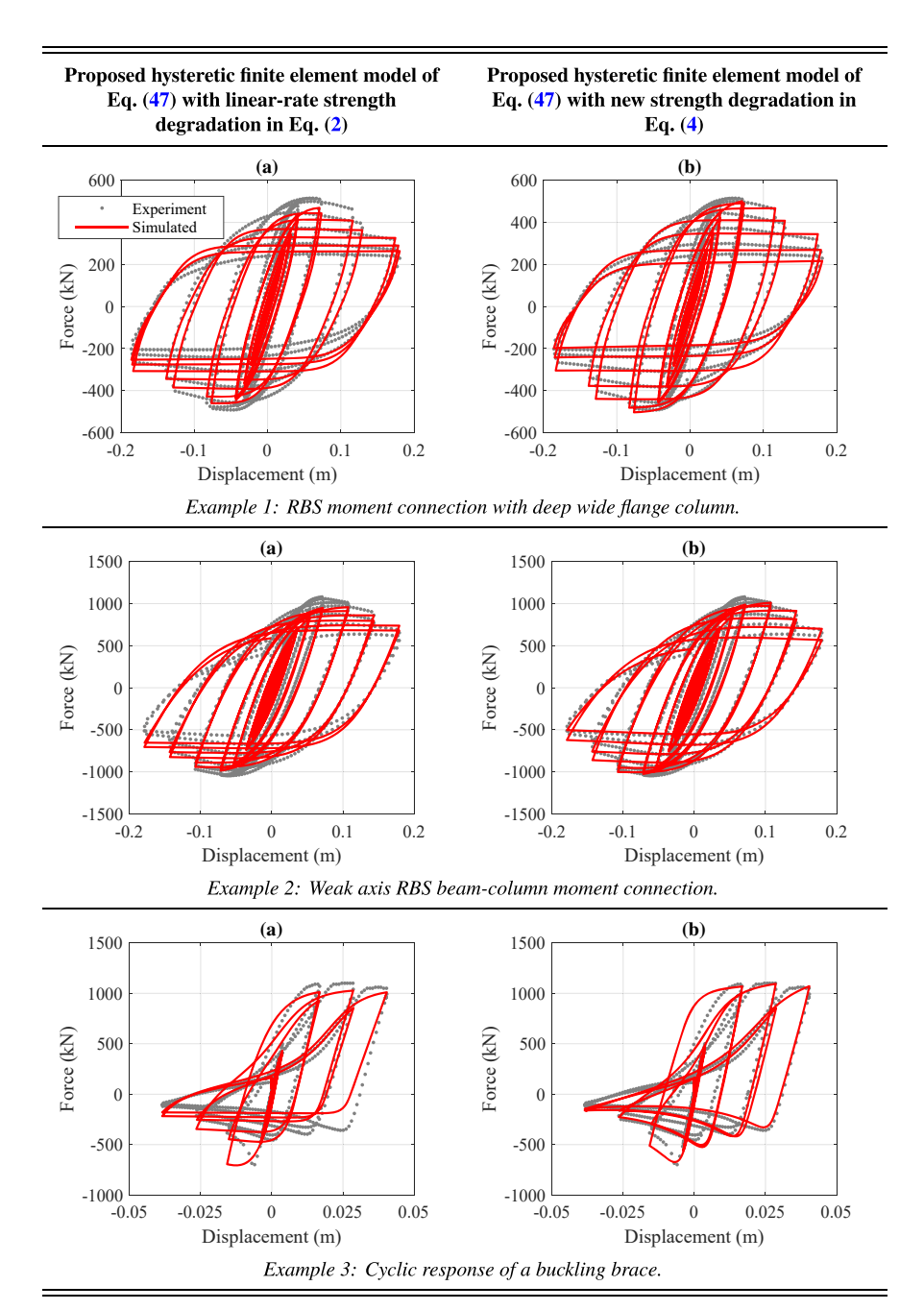


Fig. 15. Experimental verifications.

Table 1. Experimental example 1: mechanical/geometrical parameters

Parameters	E (GPa)	G (GPa)	N_p (kN)	Q_p (kN)	M_p (kNm)	$A (cm^2)$	A_s (cm ²)	$I(\text{cm}^4)$
Beam	200	77	7,238	2,300	1,951	187	100	166,076
Column	200	77	12,760	1,762	2,006	334	81	89,073

Table 2. Experimental example 1: hysteretic parameters for linear-rate strength degradation

Parameters	n	γ	α	$\delta_{ u}$	δ_{η}
Beam/column	1	2.5	0.003	1.7×10^{-6}	6×10^{-7}

Table 3. Experimental example 1: hysteretic parameters for proposed strength degradation

Parameters	n	γ	α	$\delta_{\nu 1}$	$\delta_{ u2}$	$\delta_{ u 3}$	δ_{η}
Beam/column	0.9	2.7	0.01	0.14	3.8×10^{-6}	2.2	5×10^{-7}

Table 4. Experimental example 2: mechanical/geometrical parameters

Parameters	E (GPa)	G (GPa)	N_p (kN)	Q_p (kN)	M_p (kNm)	$A (cm^2)$	A_s (cm ²)	$I(\text{cm}^4)$
Beam	200	77	10,730	3,002	3,640 2,547	285	144 545	376,273
Column	200	11	29,125	12,160	2,547	754	545	90,322

Table 5. Experimental example 2: hysteretic parameters for linear-rate strength degradation

Parameters	n	γ	α	$\delta_{ u}$	δ_{η}^{+}	δ_{η}^{-}
Beam/column	0.6	0.9	0	5.0×10^{-7}	7×10^{-7}	1.8×10^{-7}

Table 6. Experimental example 2: hysteretic parameters for proposed strength degradation

Parameters	n	γ	α	$\delta_{\nu 1}$	$\delta_{ u 2}$	$\delta_{\nu 3}$	δ_{η}^{+}	δ_{η}^{-}
Beam/column	0.6	1.0	0	0.1	1.7×10^{-6}	2.0	1×10^{-6}	4×10^{-7}

Table 7. Experimental example 3: mechanical/geometrical parameters

Parameters	E	N_p	A
Brace	200 GPa	1,042 kN	22 cm ²

elastic to plastic regime and nonuniform degradation evolution is well simulated in plot (b), as compared to the uniform evolution in plot (a).

Example 3: Cyclic Response of a Buckling Brace

The cyclic response of a steel brace is shown in the *third row* of Fig. 15, indicating asymmetric degradation phenomena (Fell et al. 2009). The experimental setup is shown in Fig. 14, wherein the related cross section involves a square hollow structural shape $101.6 \times 101.6 \times 6.4$ (HSS-1), with an effective section yield strength of 480 MPa. The length of the specimen is 3.124 m, with one end fully restrained, while the other end is subjected to a standard cyclic protocol following a symmetric displacement-based axial loading history (Gupta and Krawinkler 2002; Krawinkler et al. 2000).

The degrading hysteretic finite-element model is formulated here with just one element, having nodes at the start and end of the brace element. The model parameters are listed in Tables 7–9. For this model, it is assumed that strength degradation is only present for the compressive loading, while pinching is active only in the loading/reloading branches. Additionally, asymmetric stiffness degradation is assumed for reloading and unloading branches.

In plot (a), in the third row of Fig. 15, it is seen that the linearrate degradation is unable to capture the buckling phenomena for the compressive loading, and stiffness in same of the unloading branches are also not captured very well. On the other hand, in plot (b) buckling effects are appropriately simulated in the compressive cycles, and significantly matching simulation and experimental results are observed here, as compared to the linear-rate degradation rule.

Overall, the simulated results comparisons with these experimental outputs support the model's validity to simulate a broad range of complex physically observed hysteretic behaviors.

Conclusions

In this paper, a new multiaxial degrading hysteretic model is developed and integrated to a hysteretic finite-element framework, in order to efficiently simulate a diverse array of nonlinear and degrading structural behaviors. Toward this goal, a new strength degradation function is suggested, which is used to formulate scalar damage functions corresponding to axial force, shear force, and bending moment capacities degradations. Damage functions and multiaxial inelasticity are then introduced in the effective stress domain, following multiaxial damage-plasticity postulates, satisfying the consistency criteria of the yield/capacity surface. Different cases for multiaxial hysteretic models are presented based on model fidelity, ranging from the case when degradations and capacity interactions are assumed to be absent, to the most complex case of fully coupled degradation-plasticity model, where the yield/capacity surface is consistently evolving owing to strength degradation effects, now adequately simulated with the proposed framework. Stiffness degradation, pinching and asymmetry are also introduced, and the resulting multiaxial evolution model is then used in the overall finite-element formulation of a two-node hysteretic Timoshenko beam element. Although the proposed hysteretic model is implemented here for the hysteretic finite-element formulation of beam elements, it can also be straightforwardly employed as a constitutive law for fiber analysis, finite-element formulations of other elements, or even independently for simulating a range of hysteretic phenomena. Finally, a computationally efficient solution scheme is suggested for the hysteretic finiteelement formulation of quasi-static problems, where the system matrices do not need to be updated and the entire framework is elegantly represented by a system of ODEs, that can be solved

Table 8. Experimental example 3: hysteretic parameters for linear-rate strength degradation

Parameters	n	γ	α	$\delta_{ u}^{-}$	δ_{η}^{+}	δ_η^-	ζ_{10}^+	ζ_{20}^+	p^+	q^+
Brace	1.2	0.5	0	1.5×10^{-6}	0	1.8×10^{-5}	0.97	0.64	1.0×10^{-4}	0.1

Table 9. Experimental example 3: hysteretic parameters for proposed strength degradation

Parameters	n	γ	α	$\delta_{\nu 1}^{-}$	$\delta_{ u2}^-$	$\delta_{\nu 3}^-$	δ_{η}^{+}	δ_{η}^{-}	ζ_{10}^+	ζ_{20}^+	p^+	q^+
Brace	2.7	0.7	0.02	1	1.6×10^{-5}	350	4.5×10^{-5}	1.0×10^{-5}	0.9	0.51	1.0×10^{-4}	0.05

without the need of linearizations. Illustrative results and experimental verifications are provided to demonstrate that the suggested element satisfies exact equilibrium, degradations, and multiaxial yield/capacity surface interactions in one consistent framework, and is able to simulate a diverse range of complex physically

observed structural responses in a concise and efficient manner. Future work can include, among others, incorporation of large displacements and the assessment of the predictive capabilities of the model, i.e., accurately describing physical phenomena without a priori knowledge of the experimental/output data.

Appendix I. Element Matrices

In this appendix, the pertinent element matrices for the nonlinear Timoshenko beam element are presented (Amir et al. 2020).

$$\begin{split} \mathbf{B}_{(z)} &= \begin{bmatrix} -\frac{1}{L} & 0 & 0 & \frac{1}{L} & 0 & 0 \\ 0 & -\frac{12\alpha_{\phi}\lambda\mu'}{L} & -6\alpha_{\phi}\lambda\mu' & 0 & \frac{12\alpha_{\phi}\lambda\mu'}{L} & -6\alpha_{\phi}\lambda\mu' \\ 0 & -\frac{6\alpha_{\gamma}\mu'(L-2x)}{L^{3}} & \frac{6\alpha_{\gamma}\mu'x}{L^{2}} & \frac{4\mu'(\alpha_{\gamma}+3\lambda\alpha_{\phi})}{L} & 0 & \frac{6\alpha_{\gamma}\mu'(L-2x)}{L^{2}} & \frac{6\alpha_{\gamma}\mu'x}{L^{2}} & \frac{2\mu'(\alpha_{\gamma}-6\lambda\alpha_{\phi})}{L} \\ \end{bmatrix} \\ \mathbf{H}_{\mathbf{B}(z)} &= \begin{bmatrix} 0 & 0 & 0 & 0 & 0 & 0 & 0 \\ 0 & -\frac{(1-\alpha_{\gamma})\mu'}{2} & (1-\alpha_{\phi})\lambda\mu'L & 0 & -\frac{(1-\alpha_{\gamma})\mu'}{2} & -(1-\alpha_{\phi})\lambda\mu'L \\ 0 & \frac{3\mu'(1-\alpha_{\gamma})(L-2x)}{L^{2}} & -6\lambda\mu'(1-\alpha_{\phi})(L-2x) & \frac{3\mu'(1-\alpha_{\gamma})(L-2x)}{L} & \frac{6\lambda\mu'(1-\alpha_{\phi})(L-2x)}{L} \end{bmatrix} \\ \mathbf{K} &= \begin{bmatrix} \frac{\alpha_{\phi}AE}{L} & 0 & 0 & -\frac{\alpha_{\phi}AE}{L^{2}} & 0 & 0 & 0 \\ 0 & \frac{12\alpha_{\phi}\alpha_{\gamma}\mu'EI}{L^{2}} & \frac{6\alpha_{\phi}\alpha_{\gamma}\mu'EI}{L^{2}} & 0 & -\frac{12\alpha_{\phi}\alpha_{\gamma}\mu'EI}{L^{2}} & \frac{6\alpha_{\phi}\alpha_{\gamma}\mu'EI}{L^{2}} \\ 0 & \frac{6\alpha_{\phi}\alpha_{\gamma}\mu'EI}{L^{2}} & \frac{4\alpha_{\phi}(\alpha_{\gamma}+3\alpha_{\phi})\mu'EI}{L^{2}} & 0 & -\frac{6\alpha_{\phi}\alpha_{\gamma}\mu'EI}{L^{2}} & \frac{2\alpha_{\phi}(\alpha_{\gamma}-6\alpha_{\phi}\lambda)\mu'EI}{L^{2}} \\ -\frac{\alpha_{\phi}AE}{L} & 0 & 0 & \frac{\alpha_{\phi}AE}{L} & 0 & 0 \\ 0 & -\frac{12\alpha_{\phi}\alpha_{\gamma}\mu'EI}{L^{2}} & \frac{4\alpha_{\phi}(\alpha_{\gamma}+3\alpha_{\phi})\mu'EI}{L^{2}} & 0 & -\frac{6\alpha_{\phi}\alpha_{\gamma}\mu'EI}{L^{2}} & \frac{2\alpha_{\phi}(\alpha_{\gamma}-6\alpha_{\phi}\lambda)\mu'EI}{L^{2}} \\ 0 & \frac{6\alpha_{\phi}\alpha_{\gamma}\mu'EI}{L^{2}} & \frac{2\alpha_{\phi}(\alpha_{\gamma}-6\alpha_{\phi}\lambda)\mu'EI}{L^{2}} & 0 & -\frac{6\alpha_{\phi}\alpha_{\gamma}\mu'EI}{L^{2}} & \frac{4\alpha_{\phi}(\alpha_{\gamma}+3\alpha_{\phi}\lambda)\mu'EI}{L^{2}} \\ 0 & \frac{6\alpha_{\phi}\alpha_{\gamma}\mu'EI}{L^{2}} & \frac{2\alpha_{\phi}(\alpha_{\gamma}-6\alpha_{\phi}\lambda)\mu'EI}{L^{2}} & 0 & -\frac{6\alpha_{\phi}\alpha_{\gamma}\mu'EI}{L^{2}} & \frac{4\alpha_{\phi}(\alpha_{\gamma}+3\alpha_{\phi}\lambda)\mu'EI}{L^{2}} \\ 0 & \frac{6\alpha_{\phi}\alpha_{\gamma}\mu'EI}{L^{2}} & \frac{2\alpha_{\phi}(\alpha_{\gamma}-6\alpha_{\phi}\lambda)\mu'EI}{L^{2}} & 0 & -\frac{6\alpha_{\phi}\alpha_{\gamma}\mu'EI}{L^{2}} & \frac{4\alpha_{\phi}(\alpha_{\gamma}+3\alpha_{\phi}\lambda)\mu'EI}{L^{2}} \\ 0 & -\frac{6(1-\alpha_{\gamma})\alpha_{\phi}\mu'EI}{L^{2}} & -(1-\alpha_{\phi})\alpha_{\gamma}\mu'EI}{L} & 0 & -\frac{6(1-\alpha_{\gamma})\alpha_{\phi}\mu'EI}{L^{2}} & \frac{(1-\alpha_{\phi})\alpha_{\gamma}\mu'EI}{L} \\ 0 & -\frac{3(1-\alpha_{\gamma})\alpha_{\phi}\mu'EI}{L} & -(1-\alpha_{\phi})\alpha_{\gamma}+6\alpha_{\phi}\lambda)\mu'EI & 0 & -\frac{3(1-\alpha_{\gamma})\alpha_{\phi}\mu'EI}{L} & (1-\alpha_{\phi})\alpha_{\gamma}+6\alpha_{\phi}\lambda)\mu'EI \\ 0 & \frac{6(1-\alpha_{\gamma})\alpha_{\phi}\mu'EI}{L^{2}} & \frac{(1-\alpha_{\phi})\alpha_{\gamma}\mu'EI}{L} & 0 & \frac{6(1-\alpha_{\gamma})\alpha_{\phi}\mu'EI}{L} & (1-\alpha_{\phi})\alpha_{\gamma}+6\alpha_{\phi}\lambda)\mu'EI \\ 0 & -\frac{3(1-\alpha_{\gamma})\alpha_{\phi}\mu'EI}{L} & \frac{(1-\alpha_{\phi})\alpha_{\gamma}\mu'EI}{L} & 0 & \frac{3(1-\alpha_{\gamma})\alpha_{\phi}\mu'EI}{L} & (1-\alpha_{\phi})\alpha_{\gamma}+6\alpha_{\phi}\lambda)\mu'EI \\ 0 & -\frac{3(1-\alpha_{\gamma})\alpha_{\phi}\mu'EI}{L} & \frac{(1-\alpha_{\phi})\alpha_{\phi}\mu'EI}{L} &$$

Appendix II. Classical Multiaxial Plasticity to Hysteretic Model

In this appendix, the connection of a conveniently expressed hysteretic model to the classical plasticity theory is shown. The following governing equations need to be satisfied for a consistent multiaxial plastic flow (Simo and Hughes 1998):

1. Additive property, where the total strain vector (ε) can be decomposed into the elastic (ε^e) and plastic parts (ε^p) :

$$\boldsymbol{\varepsilon} = \boldsymbol{\varepsilon}^e + \boldsymbol{\varepsilon}^p \tag{52}$$

2. Stress-strain constitutive law, given by $\dot{\sigma} = \mathbf{D}\dot{\boldsymbol{e}}^e$, can be then expressed as:

$$\dot{\boldsymbol{\sigma}} = \mathbf{D}(\dot{\boldsymbol{\varepsilon}} - \dot{\boldsymbol{\varepsilon}}^p) \tag{53}$$

where σ is the stress vector and **D** is the elastic rigidity matrix. Note, when σ represents the resultant/generalized stress vector, as in the present case for a beam element, it constitutes axial force, shear force, and moment, while the corresponding strains are centerline axial strain, shear strain, and curvature.

The rate of change of plastic strain is governed by the following flow rule:

$$\dot{\boldsymbol{\varepsilon}}^p = \lambda \frac{\partial \Phi}{\partial \boldsymbol{\sigma}} \tag{54}$$

where λ is the flow parameter here, satisfying the Kuhn-Tucker complimentary conditions, and Φ is the yield/capacity function.

4. The consistency condition says that in the plastic regime, i.e., when $\Phi=0$, the rate of change of yield/capacity surface is 0, i.e.,

$$\dot{\Phi}(\boldsymbol{\sigma}) = 0; \quad \text{or} \quad \left(\frac{\partial \Phi}{\partial \boldsymbol{\sigma}}\right)^T \dot{\boldsymbol{\sigma}} = 0$$
 (55)

Note, $\dot{\Phi}$ is only a function of σ for a system with no hardening. In the elastic region, since $\dot{\boldsymbol{e}}^p = 0$, Eq. (53) yields $\dot{\boldsymbol{\sigma}} = \mathbf{D}\dot{\boldsymbol{e}}$, whereas, for the inelastic region, the rate of change in plastic strain is nonzero, and therefore, the stress-strain relation is obtained by following Eqs. (52)–(55). Substituting $\boldsymbol{\sigma}$ from Eq. (53) into Eq. (55), results in:

$$\left(\frac{\partial \Phi}{\partial \boldsymbol{\sigma}}\right)^T \mathbf{D}(\dot{\boldsymbol{\varepsilon}} - \dot{\boldsymbol{\varepsilon}}^p) = 0 \tag{56}$$

Next, by substituting $\dot{\boldsymbol{e}}^p$ from Eq. (54) into Eq. (56), the flow parameter can be obtained as:

$$\left(\frac{\partial \Phi}{\partial \boldsymbol{\sigma}}\right)^{T} \mathbf{D} \dot{\boldsymbol{e}} = \left(\frac{\partial \Phi}{\partial \boldsymbol{\sigma}}\right)^{T} \mathbf{D} \left(\frac{\partial \Phi}{\partial \boldsymbol{\sigma}}\right) \lambda; \quad \text{or}$$

$$\lambda = \left[\left(\frac{\partial \Phi}{\partial \boldsymbol{\sigma}}\right)^{T} \mathbf{D} \left(\frac{\partial \Phi}{\partial \boldsymbol{\sigma}}\right)\right]^{-1} \left(\frac{\partial \Phi}{\partial \boldsymbol{\sigma}}\right)^{T} \mathbf{D} \dot{\boldsymbol{e}} \tag{57}$$

By substituting the expression for λ from Eq. (57) into Eq. (54), and then the resulting expression for $\dot{\boldsymbol{e}}^p$ to Eq. (53), the following stress-strain relation is obtained in the inelastic range:

$$\dot{\boldsymbol{\sigma}} = \mathbf{D} \left(\dot{\boldsymbol{\varepsilon}} - \left[\left(\frac{\partial \Phi}{\partial \boldsymbol{\sigma}} \right)^T \mathbf{D} \left(\frac{\partial \Phi}{\partial \boldsymbol{\sigma}} \right) \right]^{-1} \left(\frac{\partial \Phi}{\partial \boldsymbol{\sigma}} \right) \left(\frac{\partial \Phi}{\partial \boldsymbol{\sigma}} \right)^T \mathbf{D} \dot{\boldsymbol{\varepsilon}} \right)$$
(58)

Therefore, the overall stress-strain law using the classical multiaxial plasticity theory can be expressed as:

$$\dot{\boldsymbol{\sigma}} = \begin{cases} \mathbf{D}(\mathbf{I} - \mathbf{R})\dot{\boldsymbol{\varepsilon}} & \text{for inelastic domain} \\ \mathbf{D}\dot{\boldsymbol{\varepsilon}} & \text{for elastic domain} \end{cases}; \quad \text{where } \mathbf{R} = \frac{(\frac{\partial\Phi}{\partial\sigma})(\frac{\partial\Phi}{\partial\sigma})^T\mathbf{D}(\frac{\partial\Phi}{\partial\sigma})}{(\frac{\partial\Phi}{\partial\sigma})^T\mathbf{D}(\frac{\partial\Phi}{\partial\sigma})} \\ (59)$$

where I is the identity matrix and R is the interaction matrix. Eq. (59) represents the final expression directly following the classical plasticity theory. Instead of employing different expressions for the elastic and inelastic regimes, Eq. (59) can be now simply transformed into the following unified law, satisfying all the aforementioned conditions for both elastic and inelastic regions:

$$\dot{\boldsymbol{\sigma}} = \mathbf{D}(\mathbf{I} - H_1 H_2 \mathbf{R}) \dot{\boldsymbol{\varepsilon}} \tag{60}$$

where $H_1 = |\Phi + 1|^n$ and $H_2 = \beta + \gamma \text{sgn}(\boldsymbol{\sigma}^T \dot{\boldsymbol{\epsilon}})$ are the appropriate functions, such that either one of them tends to zero in the elastic domain, and both reach their maximum value of 1 in the inelastic domain, providing same results as in Eq. (59). The resulting expression in Eq. (60) presents a hysteretic model without any hardening effects, as in Eq. (24). Kinematic hardening can be now externally added in the model by simply transforming Eq. (60) to:

$$\dot{\boldsymbol{\sigma}} = \boldsymbol{\alpha} \mathbf{D} \dot{\boldsymbol{\varepsilon}} + (\mathbf{I} - \boldsymbol{\alpha}) \mathbf{D} (\mathbf{I} - H_1 H_2 \mathbf{R}) \dot{\boldsymbol{\varepsilon}}$$
 (61)

where the second term on the right side of Eq. (61) represents the elastoplastic response with no hardening, while the first term adds the kinematic hardening with a slope of αD .

Hence, Eq. (61) represents the final form of the multiaxial hysteretic model, which can be very practically and concisely re-expressed as:

$$\sigma = \alpha \mathbf{D} \boldsymbol{\varepsilon} + (\mathbf{I} - \boldsymbol{\alpha}) \mathbf{D} \mathbf{z}; \qquad \dot{\mathbf{z}} = (\mathbf{I} - H_1 H_2 \mathbf{R}) \dot{\boldsymbol{\varepsilon}}$$
 (62)

where **z** can be considered as the hysteretic deformations as shown in Eqs. (18) and (26). The extension to the developed coupled degradation-plasticity formulation in the most general form can be seen in Eq. (34) and is presented in detail in this work.

Data Availability Statement

All data used during the study are available in online repositories (Al-Shawwa and Lignos 2019a, b, DesignSafe-CI 2018), and details about the experiments are originally published in Yu et al. (2000), Gilton and Uang (2002), and Fell et al. (2009), respectively. All codes generated during the study are available from the authors by request.

Acknowledgments

This material is based upon work supported by the National Science Foundation under Grant No. CMMI-1634575.

References

Al-Shawwa, N., and D. Lignos. 2019a "Web-based interactive tools for performance-based earthquake engineering." Accessed June 23, 2020. http://resslabtools.epfl.ch/steel/report.php?s_id=Uang-SSRP-00 -CW-1.

Al-Shawwa, N., and D. Lignos. 2019b "Web-based interactive tools for performance-based earthquake engineering." Accessed June 23, 2020. http://resslabtools.epfl.ch/steel/report.php?s_id=Uang-SSR-00-LS-1.

Amir, M., K. G. Papakonstantinou, and G. P. Warn. 2020. "A consistent Timoshenko hysteretic beam finite element model." *Int. J. Non Linear Mech.* 119: 103218. https://doi.org/10.1016/j.ijnonlinmec.2019.07.003.

- Andriotis, C., I. Gkimousis, and V. K. Koumousis. 2015. "Modeling reinforced concrete structures using smooth plasticity and damage models." J. Struct. Eng. 142 (2): 04015105. https://doi.org/10.1061/(ASCE)ST.1943-541X.0001365.
- Andriotis, C. P., K. G. Papakonstantinou, and V. K. Koumousis. 2018. "Nonlinear programming hybrid beam-column element formulation for large-displacement elastic and inelastic analysis." *J. Eng. Mech.* 144 (10): 04018096. https://doi.org/10.1061/(ASCE)EM.1943-7889.0001483.
- Baber, T. T., and M. N. Noori. 1985. "Random vibration of degrading, pinching systems." *J. Eng. Mech.* 111 (8): 1010–1026. https://doi.org/10.1061/(ASCE)0733-9399(1985)111:8(1010).
- Baber, T. T., and Y.-K. Wen. 1981. "Random vibration hysteretic, degrading systems." J. Eng. Mech. Div. 107 (6): 1069–1087.
- Bathe, K. J. 1996. Finite element procedures. Upper Saddle River, NJ: Prentice Hall.
- Bouc, R. 1967. "Forced vibrations of mechanical systems with hysteresis." In Proc., 4th Conf. on Nonlinear Oscillations. Prague, Czech Republic.
- Casciati, F. 1989. "Stochastic dynamics of hysteretic media." *Struct. Saf.* 6 (2–4): 259–269.
- Charalampakis, A., and V. K. Koumousis. 2009. "A Bouc–Wen model compatible with plasticity postulates." *J. Sound Vib.* 322 (4–5): 954–968. https://doi.org/10.1016/j.jsv.2008.11.017.
- Clark, P., K. Frank, H. Krawinkler, and R. Shaw. 1997. Protocol for fabrication, inspection, testing, and documentation of beam-column connection tests and other experimental specimens. Rep. No. SAC/ BD-97/02. Sacramento, CA: SAC Joint Venture.
- Deierlein, G. G., A. M. Reinhorn, and M. R. Willford. 2010. Nonlinear structural analysis for seismic design. NEHRP Seismic Design Technical Brief No. 4. Gaithersburg, MD: NIST.
- DesignSafe-CI. 2018 "NEES-2005-0096: Ultra-low cycle fatigue and fracture in steel structures." Accessed June 23, 2020. https://www.designsafe-ci.org/data/browser/public/nees.public//NEES-2005-0096.groups/Experiment-1/.
- Di Re, P., D. Addessi, and F. C. Filippou. 2018. "Mixed 3D beam element with damage plasticity for the analysis of RC members under warping torsion." *J. Struct. Eng.* 144 (6): 04018064. https://doi.org/10.1061/(ASCE)ST.1943-541X.0002039.
- Do, T. N., and F. C. Filippou. 2018. "A damage model for structures with degrading response." *Earthquake Eng. Struct. Dyn.* 47 (2): 311–332. https://doi.org/10.1002/eqe.2952.
- Erlicher, S., and N. Point. 2004. "Thermodynamic admissibility of Bouc–Wen type hysteresis models." *C.R. Mec.* 332 (1): 51–57. https://doi.org/10.1016/j.crme.2003.10.009.
- Fell, B. V., A. M. Kanvinde, G. G. Deierlein, and A. T. Myers. 2009. "Experimental investigation of inelastic cyclic buckling and fracture of steel braces." *J. Struct. Eng.* 135 (1): 19–32. https://doi.org/10 .1061/(ASCE)0733-9445(2009)135:1(19).
- Feng, D.-C., X.-D. Ren, and J. Li. 2018. "Softened damage-plasticity model for analysis of cracked reinforced concrete structures." *J. Struct. Eng.* 144 (6): 04018044. https://doi.org/10.1061/(ASCE)ST.1943 -541X.0002015.
- Feng, D.-C., G. Wu, Z.-Y. Sun, and J.-G. Xu. 2017. "A flexure-shear Timoshenko fiber beam element based on softened damage-plasticity model." *Eng. Struct.* 140 (Jun): 483–497. https://doi.org/10.1016/j .engstruct.2017.02.066.
- Foliente, G. C. 1995. "Hysteresis modeling of wood joints and structural systems." *J. Struct. Eng.* 121 (6): 1013–1022. https://doi.org/10.1061/(ASCE)0733-9445(1995)121:6(1013).
- Gendy, A. S., and A. F. Saleeb. 1993. "Generalized yield surface representations in the elasto-plastic three-dimensional analysis of frames." *Comput. Struct.* 49 (2): 351–362. https://doi.org/10.1016/0045-7949(93) 90114-S.
- Gilton, C. S., and C.-M. Uang. 2002. "Cyclic response and design recommendations of weak-axis reduced beam section moment connections." J. Struct. Eng. 128 (4): 452–463. https://doi.org/10.1061/(ASCE)0733-9445(2002)128:4(452).
- Grassl, P., and M. Jirásek. 2006. "Damage-plastic model for concrete failure." *Int. J. Solids Struct.* 43 (22–23): 7166–7196. https://doi.org/10.1016/j.ijsolstr.2006.06.032.

- Gupta, A., and H. Krawinkler. 2002. Prediction of seismic demands for SMRF's with ductile connections and elements. Rep. No. SAC/ BD-99/06. Sacramento, CA: SAC Joint Venture.
- Ibarra, L. F., R. A. Medina, and H. Krawinkler. 2005. "Hysteretic models that incorporate strength and stiffness deterioration." *Earth-quake Eng. Struct. Dyn.* 34 (12): 1489–1511. https://doi.org/10.1002/eae.495.
- Ismail, M., F. Ikhouane, and J. Rodellar. 2009. "The hysteresis Bouc-Wen model, a survey." *Arch. Comput. Methods Eng.* 16 (2): 161–188. https://doi.org/10.1007/s11831-009-9031-8.
- Kachanov, L. 1958. "Time of the rupture process under creep conditions." Izvestiya Akademii Nauk SSSR Otdelenie Tekniches 8: 26–31.
- Kachanov, M. 1980. "Continuum model of medium with cracks." J. Eng. Mech. 106: 1039–1051.
- Kottari, A., A. Charalampakis, and V. K. Koumousis. 2014. "A consistent degrading Bouc–Wen model." *Eng. Struct.* 60: 235–240. https://doi.org /10.1016/j.engstruct.2013.12.025.
- Krajcinovic, D. 1996. Vol. 41 of *Damage mechanics*. Amsterdam, Netherlands: Elsevier.
- Krawinkler, H., A. Gupta, R. Medina, and N. Luco. 2000. Loading histories for seismic performance testing of SMRF components and assemblies. Rep. No. SAC/BD-00/10. Sacramento, CA: SAC Joint Venture.
- Lemaitre, J. 1985. "A continuous damage mechanics model for ductile fracture." J. Eng. Mater. Technol. 107 (1): 83–89. https://doi.org/10.1115/1.3225775.
- Lemaitre, J. 1996. A course on damage mechanics. New York: Springer. Lignos, D. G., and H. Krawinkler. 2010. "Deterioration modeling of steel components in support of collapse prediction of steel moment frames under earthquake loading." J. Struct. Eng. 137 (11): 1291–1302. https:// doi.org/10.1061/(ASCE)ST.1943-541X.0000376.
- Lubliner, J., J. Oliver, S. Oller, and E. Onate. 1989. "A plastic-damage model for concrete." *Int. J. Solids Struct.* 25 (3): 299–326. https://doi.org/10.1016/0020-7683(89)90050-4.
- Miah, M. S., E. N. Chatzi, V. K. Dertimanis, and F. Weber. 2015. "Non-linear modeling of a rotational MR damper via an enhanced Bouc-Wen model." Smart Mater. Struct. 24 (10): 105020. https://doi.org/10.1088/0964-1726/24/10/105020.
- Papakonstantinou, K. G., P. C. Dimizas, and V. K. Koumousis. 2008. "An inelastic beam element with hysteretic damping." *Shock Vib.* 15 (3): 273–290. https://doi.org/10.1155/2008/707419.
- Scott, M. H., G. L. Fenves, F. McKenna, and F. C. Filippou. 2008. "Software patterns for nonlinear beam-column models." *J. Struct. Eng.* 134 (4): 562–571. https://doi.org/10.1061/(ASCE)0733-9445(2008) 134:4(562)
- Sengupta, P., and B. Li. 2013. "Modified Bouc–Wen model for hysteresis behavior of RC beam–column joints with limited transverse reinforcement." *Eng. Struct.* 46: 392–406. https://doi.org/10.1016/j.engstruct. 2012.08.003.
- Simo, J., and T. Hughes. 1998. *Computational inelasticity*. New York: Springer.
- Sivaselvan, M. V., and A. M. Reinhorn. 2000. "Hysteretic models for deteriorating inelastic structures." *J. Eng. Mech.* 126 (6): 633–640. https://doi.org/10.1061/(ASCE)0733-9399(2000)126:6(633).
- Sivaselvan, M. V., and A. M. Reinhorn. 2004. *Nonlinear structural analysis towards collapse simulation: A dynamical systems approach*. Technical Rep. No. MCEER-04-0005. Buffalo, NY: Univ. at Buffalo.
- Sofianos, C. D., and V. K. Koumousis. 2018. "Hysteretic beam element with degrading smooth models." *Arch. Appl. Mech.* 88 (1–2): 253–269. https://doi.org/10.1007/s00419-017-1263-8.
- Spacone, E., F. C. Filippou, and F. F. Taucer. 1996. "Fibre beam-column model for non-linear analysis of RC frames: Part I. Formulation." *Earthquake Eng. Struct. Dyn.* 25 (7): 711–725. https://doi.org/10.1002/%28SICI%291096-9845%28199607%2925%3A7%3C711%3A%3AAID-EQE576%3E3.0.CO%3B2-9.
- Triantafyllou, S. P., and V. K. Koumousis. 2011a. "An inelastic Timoshenko beam element with axial–shear–flexural interaction." *Comput. Mech.* 48 (6): 713–727. https://doi.org/10.1007/s00466-011-0616-3.
- Triantafyllou, S. P., and V. K. Koumousis. 2011b. "Small and large displacement dynamic analysis of frame structures based on hysteretic

- beam elements." *J. Eng. Mech.* 138 (1): 36–49. https://doi.org/10.1061/(ASCE)EM.1943-7889.0000306.
- Van Do, V. N. 2016. "The behavior of ductile damage model on steel structure failure." *Procedia Eng.* 142: 26–33. https://doi.org/10.1016/j .proeng.2016.02.009.
- Wang, C.-H., G. C. Foliente, M. V. Sivaselvan, and A. M. Reinhorn. 2001. "Hysteretic models for deteriorating inelastic structures." *J. Eng. Mech.* 127 (11): 1200–1202. https://doi.org/10.1061/(ASCE)0733-9399(2001) 127:11(1200).
- Wen, Y.-K. 1976. "Method for random vibration of hysteretic systems." J. Eng. Mech. Div. 102 (2): 249–263.
- Yu, B., C.-L. Ning, and B. Li. 2016. "Hysteretic model for shear-critical reinforced concrete columns." J. Struct. Eng. 142 (9): 04016056. https://doi.org/10.1061/(ASCE)ST.1943-541X.0001519.
- Yu, Q., C. Gilton, and C.-M. Uang. 2000. Cyclic response of RBS moment connections: Loading sequence and lateral bracing effects. Rep. No. SSR-99/13. La Jolla, CA: Univ. of California at San Diego.